IEEE TRANSACTIONS ON POWER ELECTRONICS, VOL. 40, NO. 9, SEPTEMBER 2025 13383

Unified Control Scheme Based on Model Predictive Control for Hybrid-Energy-Storage-Based Microgrids

Kuldeep Kumar, Chaeeun Lee, and Sungwoo Bae, *Member, IEEE*

***Abstract*—This article proposes unified hierarchical control for power distribution among ac microgrids based on hybrid energy storage. In this article, each microgrid comprises hybrid energy storage (i.e., supercapacitor, battery, and hydrogen) and renewable power generator (i.e., photovoltaic module). The proposed hierarchical control framework ensures that power distribution among microgrids depends on the state of charge (SOC) of hybrid storage in the given microgrids. The present article proposes an adaptive model predictive control based tertiary layer, which is responsible for the accurate power-sharing among the microgrids based on the individual SOC of the storages in the given microgrids. The tertiary control layer generates the reference signals for the secondary control layer, where the pulsewidth modulation of the inverters in the respective microgrids is controlled. The primary control is responsible for the optimum power-sharing within individual microgrids based on the source, load, and SOC of energy storage devices. The proposed unified hierarchical control for such a system is validated in different operating scenarios using power hardware-in-the-loop experiments. The proposed control scheme is very effective in smooth and controlled power exchange among microgrids during fuel cell operating mode. The proposed scheme also improves the dc bus regulation during transient power imbalances in microgrids.**

***Index Terms*—Fuel cell (FC), hydrogen energy, microgrids cluster, model predictive control (MPC), power converters.**

NOMENCLATURE

Bat	Battery.
C	Capacity of energy storage.
C_s	Inverter filter capacitance.
ECR	Equal concern for relaxation.
ESS	Energy storage system.
Hyd	Hydrogen.
K_I	Integral gain.
K_P	Proportional gain.
$L.O.$	Luenberger observer.
L_s	Inverter filter inductance.
$L_{t1,2}$	Inductance of transmission line.
MHL	Metal hydride storage level.
MPC	Model predictive control.
MPPT	Maximum power point tracking.
MV	Manipulative variable.
N	Horizons.
OV	Output variable.
P	Active power.
PLL	Phased-lock loop.
$P_{\mathrm{Net,ref}}$	Power reference signal in microgrid.
$P_{\mu G}$	Power exchange between microgrid.
Q	Reactive power.
R_o	Load resistance.
$R_{t1,2}$	Resistance of transmission line.
SC	Supercapacitor.
SFC	Secondary frequency control.
SOC	State of charge.
SVC	Secondary voltage control.
t_d	Delay time.
T_{onset}	Scenario onset time.
T_s	Sample time.
VSI	Voltage source inverter.
V_{ac}	Voltage of voltage source inverter (V).
V_r	Receiving end voltage (V).
V_s	Source voltage (V).
X	Line inductance (H).

Subscript and superscripts

k	Sampling instant.
m	Measured.
Net	Net reference.
Nom.	Nominal.
p	Prediction horizon and predicted.
Second,ref	Secondary controller reference.
t	Time.
Y	Output.
μG	Microgrid.

Received 18 October 2024; revised 17 January 2025; accepted 8 March 2025. Date of publication 17 March 2025; date of current version 30 June 2025. This work was supported in part by the Korea Institute of Energy Technology Evaluation and Planning (KETEP) and the Ministry of Trade, Industry & Energy (MOTIE) of the Republic of Korea under Grant 20225500000060, in part by the Operation System for AC/DC Hybrid Distribution Networks under Grant RS-2024-00422103, and in part by the EV Smart Charging Platform Innovation Research Center. Recommended for publication by Associate Editor Z. Chen. *(Corresponding author: Sungwoo Bae.)*

Kuldeep Kumar is with the Indian Institute of Technology Guwahati, Guwahati 781039, India (e-mail: kuldeepk@iitg.ac.in).

Chaeeun Lee and Sungwoo Bae are with the Department of Electrical Engineering, Hanyang University, Seoul 04763, South Korea (e-mail: codmseun@hanyang.ac.kr; swbae@hanyang.ac.kr).

Color versions of one or more figures in this article are available at https://doi.org/10.1109/TPEL.2025.3552210.

Digital Object Identifier 10.1109/TPEL.2025.3552210

1,2	Denotes the power exchange between 1 and 2.
1,3	Denotes the power exchange between 1 and 3.

Greek symbols

α_i	Weight on the manipulative variables and proportional gain for power sharing in tertiary layer.
β_i	Weight on the variations of manipulative variables.
γ_i	Weight on the output error.
δ	The phase angle between two voltage sources.
ζ	Conversion coefficients.
η	Efficiency.
μG1,2,3	Microgrids 1, 2, and 3, respectively.
ρ	Weight on the control effort.
Δ	Difference.

I. INTRODUCTION

MICROGRIDS (μGs) are generally defined as a group of power generators, energy storage units, and distributed loads as a single controllable entity that can function in standalone and grid-connected mode [1]. The fact that μGs can have better power quality, higher power conversion efficiencies, and economic benefits can be foreseen as a key entity in future electricity networks globally [2]. The control and operation of μGs, considering the operational characteristics of renewable power generators (RPGs) and energy storage systems (ESSs) along with load management, have been the central idea of research in the last decade [3]. The μGs can also be configured as a cluster of different μG units to facilitate a better electricity network but a complex controllable system [4].

In the past, several studies have been attempted in the control and operation of a cluster of μGs. Secondary power management was proposed for an ac μG cluster using the two-layer cooperative framework. The secondary controller facilitated the optimum power among distributed energy resources (DERs) in each μG and economic power dispatch among the μG group [5]. A cluster-oriented control was proposed for the ac μGs cluster. The intercluster scheme was responsible for the optimum power sharing among μGs, while the intracluster manages the frequency and voltage of the DERs in each μG [6]. A study was presented on pinning-based hierarchical and distributed cooperative control strategies for the ac μG cluster [7]. A tube-model predictive control (MPC) was proposed for the offgrid μGs clusters. A mixed-stage optimization was used in which the control objective was optimized progressively at diverse energy management scales and prediction horizons [8]. Unified coordinated power control for the dc μGs cluster was proposed using an isolated bidirectional dc–dc converter [9].

In another article, effective power-sharing was presented among the μGs for networked ac and dc μGs using a set of interconnected converters [10]. An event-based distributed census control was used in the power-sharing method. In this method, each interconnected converter worked as an agent that required the information of its local and neighboring converters [10]. A study was performed on the modeling, analysis, and stabilization of the photovoltaic (PV)-based μG cluster [11]. A distributed voltage control and power management of networked μGs was studied. In this article, a two-level control framework was used [12]. A unified hierarchical control was proposed for tie-line power flow between the dc μGs. In this control scheme, the pinning strategy is unified with distributed optimization and average voltage regulation control loops [13]. A tertiary control for a cluster of dc μGs was presented. The proposed controller was very useful for the maximum utilization of renewable power, minimum stress and aging of components, and maintenance cost [14]. In another article, supervisory coordinated control was proposed for the fuel cell (FC) based dc μGs cluster based on the multiagent system. However, the concept of hybrid ESS and its effect on power distribution were not studied for the dc μGs cluster [15]. A dc power exchange highway-based power-sharing method was proposed for the dc μGs cluster [16].

Advanced control scheme such as MPC have shown their usefulness in the control and operation of the hybrid ESS-based μGs system [1], [17], [18]. An MPC has been used for the system-level control of the PV and battery ESS [19], [20], [21]. These studies showed that the MPC is a very effective control method for μGs considering operational cost, durability, better power quality, and voltage stability. A model predictive voltage control based control was studied for the renewable-energy-based μGs without a proportional–integral–derivative (PID) controller. It was found that the proposed work improved the dynamic performance of the μG as compared to the PID controller [22]. An MPC-based current control for a bidirectional three-level dc/dc converter was proposed for hybrid energy storage based dc μGs. However, hydrogen storage characteristics were not considered in the article [23]. In another article, a study was proposed on a finite control set MPC-based control for the fast and reliable operation of the ac μGs. The proposed control strategy improved the voltage tracking capacity of the power converters [24]. A review was presented on the multiagent-based distributed control and optimization in the μG cluster. It was observed that communication delay can significantly affects the overall performance of the μG system [25]. A network fuzzy predictive control of the network μGs was studied for the dynamic voltage stabilization of the dc μGs. It was found that the proposed method showed better robustness as compared to the conventional method [26]. In another article, an adaptive dynamic reference control was proposed for the power converter for μG applications. The proposed control strategy showed better convergence to its nominal reference even in the presence of the model parameter uncertainty, sensor imperfections, and unmodeled dynamics [27]. A computationally efficient MPC was studied for dual-output multilevel converters for μG applications. It was found that the proposed method improved the system's performance by reducing the computational burden and achieving multivariable control [28]. In another article, a passivity-based partial sequential MPC was studied for grid-connected applications. The proposed control scheme enhanced the antidisturbance abilities and achieved resonance suppression [29]. An ultralocal predictive control was proposed for the grid-connected application using the sliding mode disturbance observer. It was found proposed control method outperformed the conventional methods [30]. A model-free-based predictive control was proposed for the grid-forming applications.

The proposed control scheme showed effective regulation of the grid-forming inverter without the knowledge of the physical model [31]. A review study was performed on the control strategies for the power converters in μGs. It was found that MPC is very effective for the better performance of power quality improvements in the μGs [32].

It may be concluded that a significant amount of research has been carried out on the power distribution in the μG cluster using different control schemes, such as hierarchical and distributed control methods. However, according to the aforementioned literature review, there is an information gap in the control and power management of a μG cluster with hybrid ESS. The different devices in the hybrid ESS (supercapacitor, battery, and hydrogen) have different energy efficiency, overcharging, and deep discharging limits. In addition, the difference in the state of charge (SOC) of ESS in different μGs indicates relative energy surplus or deficit in the μGs. Therefore, a more appropriate control scheme can facilitate power distribution among the μGs depending on the SOC of a given ESS. By doing so, the differences in energy surplus or deficit in different μGs can be taken care of. For example, the μG with a higher battery SOC should deliver higher power than the other μG which has a lower SOC. The different ESSs may also be active (based on working SOC) at a given operating time in different μGs. For example, in a cluster group of three μGs, μG2 can have battery SOC in the working range (40%–80%) while μG3 does not have battery SOC in the operational range instead hydrogen storage is in the working range (20%–90%). Therefore, power sharing based on SOC of ESS in different μGs becomes interesting considering the energy efficiency and response time of ESS. Here, it is worth mentioning that energy management in the given μG is performed based on the SOC of ESS; therefore, at a time, only one storage is active either hydrogen or battery [33].

It can be summarized that control strategies used in the literature have limitations in that they are unable to facilitate the power-sharing among the μGs cluster based on the SOCs of hybrid energy storage, constraints on the SOC_S of hybrid ESS, power output, and rate of power change of devices. Therefore, the proposed control strategy addresses the aforementioned limitations of the existing control methods using the adaptive MPC-based tertiary control layer which facilitates the power-sharing based on the SOCs of hybrid ESS, handles the constraints on power and rate of power change of devices, and limits on the SOCs of hybrid ESS. A complete closed-loop control of the tertiary layer with secondary and primary layers is presented for such a hybrid ESS-based system which is missing in the literature. Table I summarizes how the proposed control improves the limitations of the previous articles.

In the present article, the problem statement is that power-sharing among μGs should be driven by the SOC of the hybrid ESS of respective μGs, where each μG in the cluster has hybrid energy storage (SC, battery, and hydrogen). To the best of the author's knowledge, this kind of system (μG cluster based on hybrid ESS) and the given problem statement have not been addressed in the previous articles. In addition, the power-sharing is achieved in ac μGs; therefore, a suitable control mechanism is developed for controlling the inverters using different control layers framework. Therefore, the contributions of the present article are a unique problem statement and the development of a dedicated control mechanism to achieve the desired objectives. Applications of such type of ESS in μG become a multi-input and multioutput system subjected to various operating constraints. Owing to the multi-input and multioutput plant subjected to multiple physical constraints on the power limit, rate of power change, and SOC, this kind of system needs a smart control scheme that can handle the multiple constraints and facilitate the desired response. Considering the suitability and advantages of the MPC for the multi-input and multiunit plant with multiple physical constraints, the authors used MPC in a hierarchical control (primary, secondary, and tertiary layers) framework. In this hierarchical control framework, each layer of control optimizes the control variables while fulfilling the various constraints and tracking the reference values. Further, the adaptive MPC capability has been used to ensure the SOC-based proportional power-sharing among the μGs while the SOCs of battery and hydrogen storage vary in real-time. The major contributions of the present article can be summarized as follows.

TABLE I
MAJOR CONTRIBUTION IN COMPARISON WITH STATE-OF-ART

	[5]	[6]	[7]	[9]	[10]	[12]	[13]	[15]	[34]	Proposed
Feature [1]	No	No	No	No	No	No	No	Yes	No	Yes
Feature [2]	No	No	No	No	No	No	No	No	No	Yes
Feature [3]	No	No	No	No	No	No	No	No	No	Yes
Feature [4]	Yes	Yes	Yes	No	Yes	Yes	No	No	No	Yes

*Feature [1] – Power sharing in μGs based on SOCs considering hybrid ESS.
Feature [2] – Complete closed-loop analysis based on MPC-based primary. secondary, and tertiary layers and transient performance analysis.
Feature [3] – Application of adaptive MPC in the tertiary layer.
Feature [4] – Power sharing between ac μGs.

1) Development of a control strategy for a cluster of hybrid energy storage-based μGs in which power exchange among μGs is governed by the SOCs of hybrid ESS of respective μGs. This control scheme renders the minimization of SOC difference between μGs.
2) To obtain the set objectives and control the given multi-input and multioutput μGs system subjected to various operating constraints (SOC and rate of power change), a hierarchical control framework (primary, secondary, and tertiary) is developed.
3) The tertiary control layer is responsible for optimizing the reference signals for the power exchange among μGs. The different operating modes are defined based on the SOCs of ESS in different μGs (Algorithm 1. Selection of the operating modes in the tertiary layer).
4) The secondary layer of the hierarchical control scheme ensures the effective control of the inverters (connected in cluster as shown in Fig. 2) for the power flow control and facilitating the plug-and-play and facilitating the plug-and-play capability in the μGs cluster.
5) The dynamic performance analysis of the proposed integrated hierarchical control framework (tertiary controller, secondary controller, and primary controller is evaluated in different operating scenarios using power hardware-in-the-loop (PHIL) experiments.

Algorithm 1: Selection of the operating modes in tertiary layer.

```
Mode 1 Condition 1
    IF$(P_{\mathrm{Net,ref}} >= 0)\&\&(SOC_{\mu G2} >= 42)\&\&(SOC_{\mu G2} <= 78)\&\&(SOC_{\mu G3} >= 42)\&\&(SOC_{\mu G3} <= 78)\&\&(MHL_{\mu G2} >= 20)\&\&(MHL_{\mu G2} <= 90)\&\&(MHL_{\mu G3} >= 20)\&\&(MHL_{\mu G3} <= 90)$
Mode 2 Condition 2
    IF $(P_{\mathrm{Net,ref}} < 0)\&\&(SOC_{\mu G2} >= 42)\&\&(SOC_{\mu G2} <= 78)\&\&(SOC_{\mu G3} >= 42)\&\&(SOC_{\mu G3} <= 78)\&\&(MHL_{\mu G2} >= 20)\&\& (MHL_{\mu G2} <= 90)\&\&(MHL_{\mu G3} >= 20)\&\&(MHL_{\mu G3} <= 90)$
Mode 3 Condition 3
    IF $(P_{\mathrm{Net,ref}} < 0)\&\&(SOC_{\mu G2} >= 42)\&\&(SOC_{\mu G2} <= 78)\&\&((SOC_{\mu G3} < 42)\|(SOC_{\mu G3} > 78))\&\&(MHL_{\mu G2} >= 20)\&\&(MHL_{\mu G2} <= 90)\ \&\&\ (MHL_{\mu G3} >= 20)\&\&(MHL_{\mu G3} <= 90)$
Mode 4 Condition 4
    IF $(P_{\mathrm{Net,ref}} < 0)\&\&((SOC_{\mu G2} < 42)|(SOC_{\mu G2} > 78))\&\&(SOC_{\mu G3} >= 42)\&\&(SOC_{\mu G3} <= 78)\&\&(MHL_{\mu G2} >= 20)\&\&(MHL_{\mu G2} <= 90)\&\&(MHL_{\mu G3} >= 20)\&\&(MHL_{\mu G3} <= 90)$
Mode 5 Condition 5
    IF $(P_{\mathrm{Net,ref}} > 0)\&\&((SOC_{\mu G2} < 42)\|(SOC_{\mu G2} > 78))\&\&((SOC_{\mu G3} < 42)\|(SOC_{\mu G3} > 78))\&\&(MHL_{\mu G2} >= 20)\&\&(MHL_{\mu G2} <= 90)\ \&\&\ (MHL_{\mu G3} >= 20)\&\&(MHL_{\mu G3} <= 90)$
Mode 6 Condition 6
    IF $(P_{\mathrm{Net,ref}} > 0)\ \&\&\ (SOC_{\mu G2} >= 42)\ \&\&\ (SOC_{\mu G2} <= 78)\ \&\&((SOC_{\mu G3} < 42)\|(SOC_{\mu G3} > 78))\&\&(MHL_{\mu G2} >= 20)\ \&\&\ (MHL_{\mu G2} <= 90)\&\&(MHL_{\mu G3} >= 20)\&\&(MHL_{\mu G3} <= 90)$
Mode 7 Condition 7
    IF $(P_{\mathrm{Net,ref}} > 0)\ \&\&\ (SOC_{\mu G2} < 42)\ \&\&\ ((SOC_{\mu G2} > 78)\|(SOC_{\mu G3} >= 42))\&\&(SOC_{\mu G3} <= 78)\&\&(MHL_{\mu G2} >= 20)\ \&\&\ (MHL_{\mu G2} <= 90)\&\&(MHL_{\mu G3} >= 20)\&\&(MHL_{\mu G3} <= 90)$
Mode 8 ELSE
```

Table I provides a concise summary of the comparison of the present article with the current state of the art.

The rest of this article is organized as follows. Section II explains the system description. Section III describes the methodology. Section IV explains the results. Finally, Section V concludes this article.

II. SYSTEM DESCRIPTION

In the proposed μG cluster, three μGs (μG1, μG2, and μG3) are considered. Each μG has RPG, hybrid ESS (SC, battery, and hydrogen), and loads as shown in Fig. 1. These μGs are connected using transmission lines based on resistive and inductive elements as shown in Fig. 2. Each μG has supervisory and local control for the optimal power allocation among its components, such as PV, battery, SC, FC, and the grid as shown in Fig. 3. This is referred to as primary control in this article. The working of the primary layer is presented in Section III-C. There is a tertiary controller that is responsible for the power exchange among the μGs based on the different operating modes of power management (described in the methodology Section III-A in detail). Tertiary control generates the control signals for the secondary controller. The adaptive MPC approach is used in the tertiary controller in unified control. In the secondary control, the SPWM of the voltage source inverters (VSIs) of each μG is controlled as shown in Fig. 4. The working of the secondary layer is described in Section III-B. The control scheme in the tertiary layer is shown in Fig. 5.

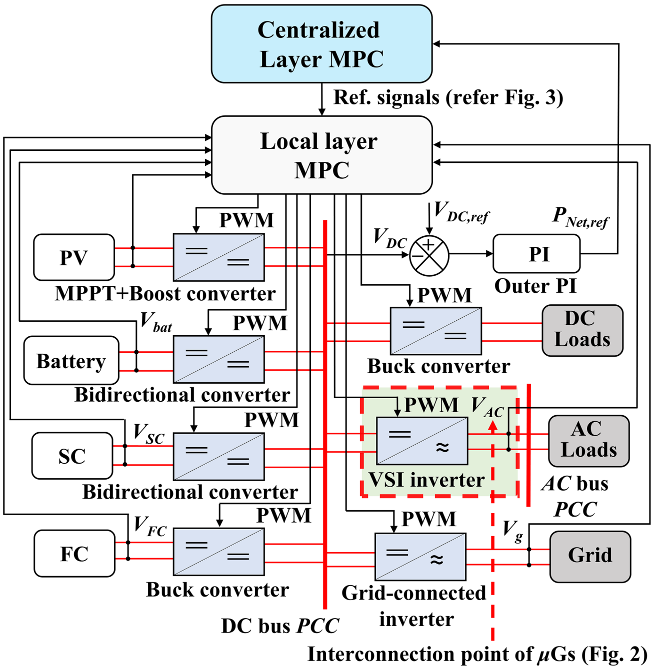

Fig. 1. Internal structure of the hybrid ESS-based μG with MPC in the present article.

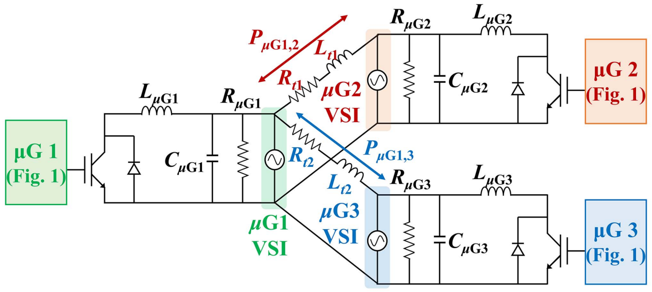

Fig. 2. Schematic of a cluster of μGs in the present article.

III. UNIFIED CONTROL STRATEGY

This section explains the working of the unified control strategy based on hybrid ESS-based μGs.

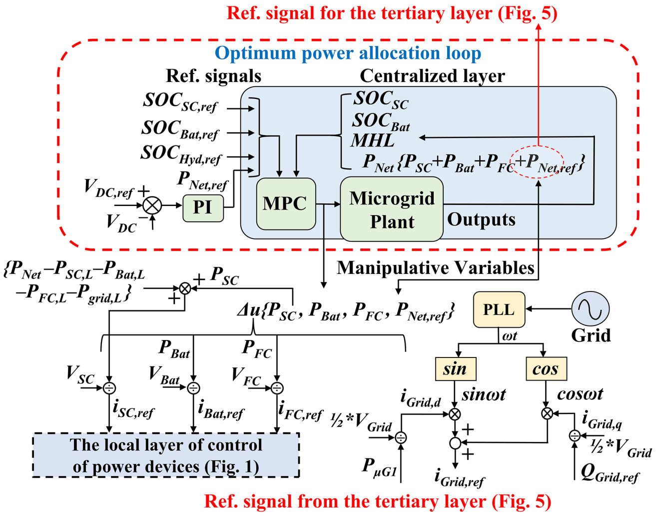

Fig. 3. Control structure of the primary control layer.

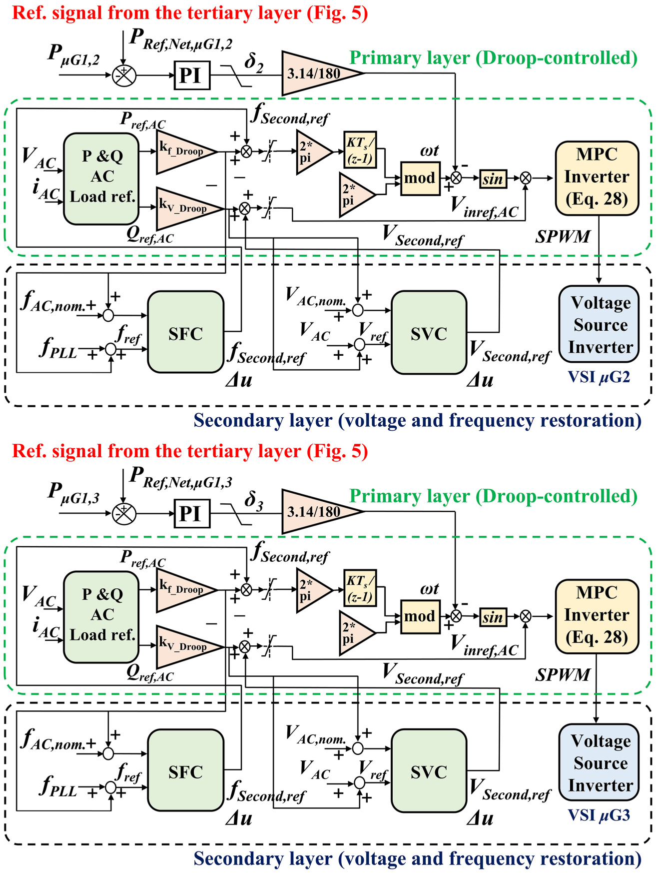

Fig. 4. Control structure of the secondary control layer.

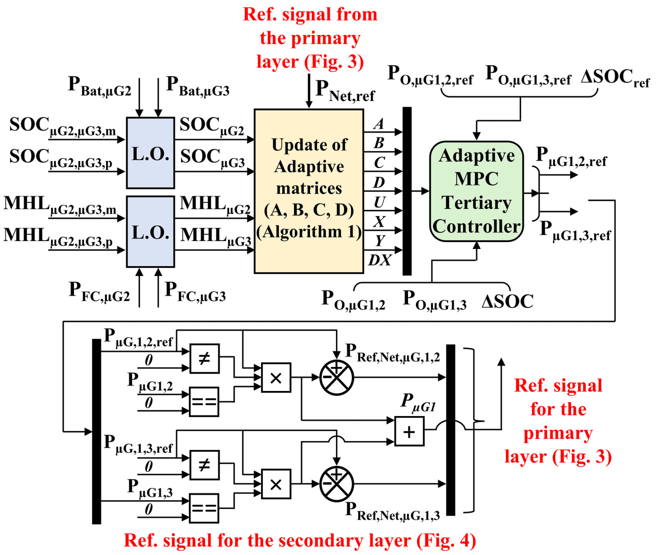

Fig. 5. Control structure of the tertiary control layer.

A. Tertiary Layer of Control

The primary objective of the tertiary control is to generate the reference signals for the power exchange ($P_{\mu G1,2}$ and $P_{\mu G1,3}$) in μGs based on the SOC values of the ESSs in the μGs. These reference signals are used by the secondary control layer. For example, if the SOCs of the battery storage in μG1 and μG2 are in the working range (40%–80%), then power flow $P_{\mu G1,2}$ and $P_{\mu G1,3}$ is proportional to the SOC of the battery storage in μG1 ($SOC_{\mu G1}$) and μG1 ($SOC_{\mu G2}$).

For ensuring the perfect power balance in the μG1, the net power reference signal can be provided as follows:

$$P_{\text{Net,ref}} = P_{\mu G1,2.\text{ref}} + P_{\mu G1\,,3,\text{ref}} \tag{1}$$

where $P_{\mu G1,2,\text{ref}}$ and $P_{\mu G1,3,\text{ref}}$ are the reference signals for power exchange between μG1 and μG2; and μG2 and μG3, respectively.

During power deficit conditions (generation<load), ($P_{\text{Net,ref}} > 0$), the relation between the $P_{\mu G1,2}$ and $P_{\mu G1,3}$ is required to be proportional to the $SOC_{\mu G2}$ and the SOC of the battery storage in μG3 ($SOC_{\mu G3}$). That means if the μG2 has a lower SOC value than μG3, μG2 should deliver lower power to μG1 as compared to the μG3. It can be formulated as follows:

$$\frac{P_{\mu G1,2.\text{ref}}}{P_{\mu G1,3,\text{ref}}} = \frac{\text{SOC}_{\mu G2}}{\text{SOC}_{\mu G3}}. \tag{2}$$

Therefore, using (1) and (2), it can be derived as follows:

$$P_{O,\mu G1,2} = P_{\mu G1,2,\text{ref}}\left(1 + \frac{\text{SOC}_{\mu G3}}{\text{SOC}_{\mu G2}}\right) \tag{3}$$

and

$$P_{O,\mu G1,3} = P_{\mu G1,3,\text{ref}}\left(1 + \frac{\text{SOC}_{\mu G2}}{\text{SOC}_{\mu G3}}\right) \tag{4}$$

where $P_{O,\mu G1,2}$ and $P_{O,\mu G1,3}$ are the outputs of the adaptive MPC while $P_{\mu G1,2}$ and $P_{\mu G1,3}$ are the manipulative variables. $P_{\text{Net,ref}}$ (Fig. 1) equals to $P_{O,\mu G1,2}$ and $P_{O,\mu G1,3}$.

During power surplus conditions (generation>load), ($P_{\text{Net,ref}} < 0$), the relation between the $P_{\mu G1,2}$ and $P_{\mu G1,3}$ is desired to be inversely proportional to $\text{SOC}_{\mu G2}$ and $\text{SOC}_{\mu G3}$

$$\frac{P_{\mu G1,2,\text{ref}}}{P_{\mu G1,3,\text{ref}}} = \frac{\text{SOC}_{\mu G3}}{\text{SOC}_{\mu G2}}. \tag{5}$$

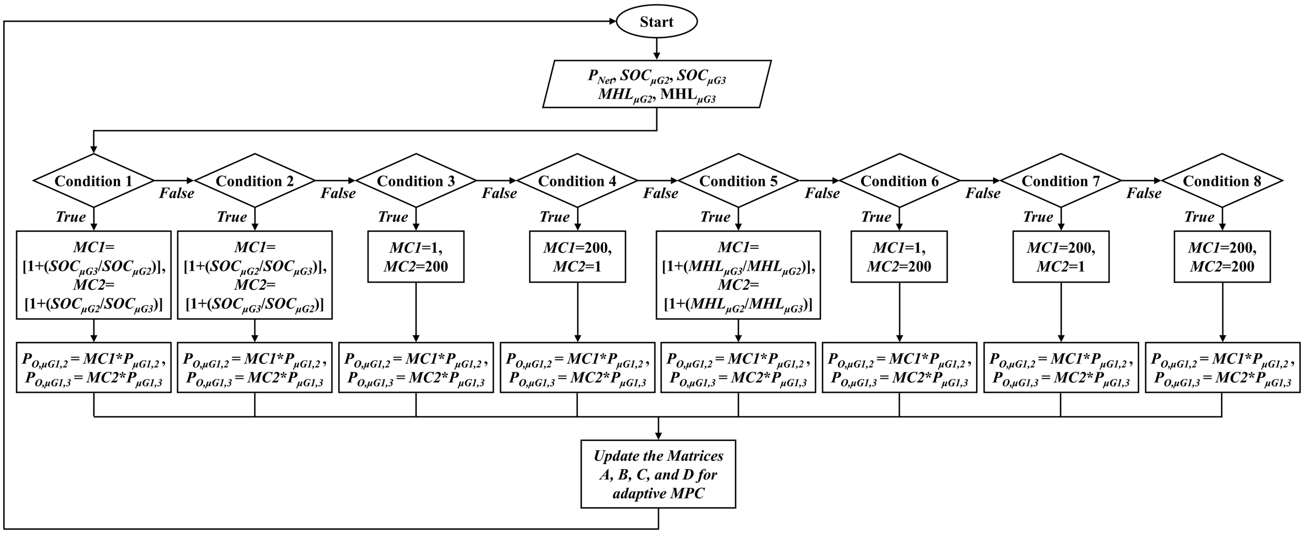

Fig. 6. Flow chart of the control Algorithm 1. Selection of the operating modes in the tertiary layer (in the algorithm, $P_{\mu G1,2}$ *refers to* $P_{\mu G1,2,ref}$, and $P_{\mu G1,3}$ refers $P_{\mu G1,3,ref}$).

Therefore, using (1) and (5), it can be formulated as follows:

$$P_{O,\mu G1,2} = P_{\mu G1,2,\text{ref}} \left(1 + \frac{\text{SOC}_{\mu G2}}{\text{SOC}_{\mu G3}}\right) \tag{6}$$

$$P_{O,\mu G1,3} = P_{\mu G1,3,\text{ref}} \left(1 + \frac{\text{SOC}_{\mu G3}}{\text{SOC}_{\mu G2}}\right). \tag{7}$$

Similarly, in case the SOC of battery storage is lower than (40%), then hydrogen storage becomes active corresponding to FC operation. Then, power flow among the μGs should be proportional to the metal hydride storage level (MHL) of the hydrogen tanks of respective μGs.

Therefore, in case μG2 and μG3 both have hydrogen storage in the working range, then it can be formulated as follows:

$$\frac{P_{\mu G1,2,\text{ref}}}{P_{\mu G1,3,\text{ref}}} = \frac{\text{MHL}_{\mu G2}}{\text{MHL}_{\mu G3}} \tag{8}$$

where $\text{MHL}_{\mu G2}$ and $\text{MHL}_{\mu G3}$ are the MHL of the hydrogen tanks in μG2 and μG3, respectively. Therefore, using (1) and (8), it can be derived as follows:

$$P_{O,\mu G1,2} = P_{\mu G1,2,\text{ref}} \left(1 + \frac{\text{MHL}_{\mu G3}}{\text{MHL}_{\mu G2}}\right) \tag{9}$$

and

$$P_{O,\mu G1,3} = P_{\mu G1,3,\text{ref}} \left(1 + \frac{\text{MHL}_{\mu G2}}{\text{MHL}_{\mu G3}}\right). \tag{10}$$

Following the inferences of (1)–(10), the different operating modes are defined based on the values of SOC and MHL in different μGs. The details of different operating modes in the tertiary layer are provided in the selection of the operating modes in the tertiary layer algorithm. The term P_{Net} in the selection of the operating modes in the tertiary layer algorithm captures the difference in the power generation and load demand. Therefore, other possible operating modes exist, and the relationships among different variables are provided in the selection of the operating modes in the tertiary layer algorithm.

Considering the (3), (4), (6), (7), (9), and (10), the desired power allocation among μGs can be achieved only when the SOC and MHL values of the storages are updated in real-time operation. Here is the usefulness of the adaptive MPC can be applied. In adaptive MPC, the plant state–space matrices can be updated at each sampling instant and the change in the plant dynamics due to parameter variations can be captured. In the proposed tertiary layer of control, the power distribution among μGs requires that values of SOC and MHL for given μGs should be updated at each sampling time. In this way, the state–space model of the plant is updated at each sampling time. Therefore, an adaptive MPC is developed, which facilitates the required power sharing among the μGs cluster.

In the case of adaptive MPC, nominal operating points are updated at each sampling time as per the requirement, which is consistent with the updated model of the plant. It can be presented as follows:

$$x(k+1) = \bar{x} + A(x(k) - \bar{x}) + B(u_t(k) - \bar{u}_t) + \Delta\bar{x} \tag{11}$$

and

$$y(k) = \bar{y} + C(x(k) - \bar{x}) + D(u_t(k) - \bar{u}_t) \tag{12}$$

where A, B, C, and D are the plant model matrices to be updated in run-time due to nonlinearity or time-varying characteristics. $\bar{x}$, $\bar{y}$, $\overline{u_t}$, and $\Delta\bar{x}$ are the nominal states, nominal outputs, nominal inputs, and nominal state increments, respectively.

In adaptive MPC, a linear-time-varying Kalman filter is used to estimate the gains L and M at each control interval which is done by the inbuilt facility in the MATLAB Simulink [35]. The value of the gain L_k and M_k can be calculated as follows [35]:

$$L_k = \left(A_k P_{k|k-1} C_{m,k}^T + N\right) \left(C_{m,k} P_{k|k-1} C_{m,k}^T + R\right)^{-1} \tag{13}$$

$$M_k = P_{k|k-1} C_{m,k}^T \left(C_{m,k} P_{k|k-1} C_{m,k}^T + R\right)^{-1} \tag{14}$$

$$P_{k+1|k} = A_k P_{k|k-1} A_m^T - \left(A_k P_{k|k-1} C_{m,k}^T + N\right) L_k^T + Q \tag{15}$$

where A_k and $C_{m,k}$ are the state–space matrices updated with time interval *k*. *R*, *N*, and *Q* are the state covariance matrices. $P_{k|k-1}$ is the state-estimation error covariance matrix estimated at the time interval $k-1$.

In a conventional MPC controller, the system plant mode is linearized at a nominal operating point to obtain the LTI approximation. The state–space model at the nominal operating point (considering the 50% value of SOC and MHL) of the tertiary layer of control based on the MPC is derived as follows:

$$\begin{aligned} \begin{bmatrix} \dot{P}_{\mu sG1,2,\text{ref}} \\ \dot{P}_{\mu sG1,3,\text{ref}} \\ \Delta \dot{\text{SOC}} \end{bmatrix} &= \begin{bmatrix} 0 & 0 & 0 \\ 0 & 0 & 0 \\ 0 & 0 & 1 \end{bmatrix} \begin{bmatrix} P_{\mu G1,2,\text{ref}} \\ P_{\mu G1,3,\text{ref}} \\ \Delta\text{SOC} \end{bmatrix} \\ &\quad + \begin{bmatrix} 1 & 0 \\ 0 & 1 \\ \zeta T_s/C & -\zeta T_s/C \end{bmatrix} \begin{bmatrix} P_{\mu G1,2,\text{ref}} \\ P_{\mu G1,3,\text{ref}} \end{bmatrix} \end{aligned} \tag{16}$$

$$\begin{aligned} \begin{bmatrix} P_{O,\mu G1,2} \\ P_{O.\mu G1,3} \\ \Delta\text{SOC} \end{bmatrix} &= \begin{bmatrix} \text{MC1} & 0 & 0 \\ 0 & \text{MC2} & 0 \\ 0 & 0 & 1 \end{bmatrix} \begin{bmatrix} P_{\mu sG1,2,\text{ref}} \\ P_{\mu sG1,3,\text{ref}} \\ \Delta\text{SOC} \end{bmatrix} \\ &\quad + \begin{bmatrix} 0 & 0 \\ 0 & 0 \\ 0 & 0 \end{bmatrix} \begin{bmatrix} P_{\mu G1,2,\text{ref}} \\ P_{\mu G1,3,\text{ref}} \end{bmatrix}. \end{aligned} \tag{17}$$

Therefore, state–space matrices can be obtained as follows:

$$\begin{aligned} A &= \begin{bmatrix} 0 & 0 & 0 & 0 \\ 0 & 0 & 0 & 0 \\ 0 & 0 & 1 & 0 \\ 0 & 0 & 1 & 0 \end{bmatrix}, B = \begin{bmatrix} 1 & 0 \\ 0 & 1 \\ 0 & 0.0002441 \\ 0 & 0 \end{bmatrix}, \\ C &= \begin{bmatrix} 1.5 & 0 & 0 & 0 \\ 0 & 1.5 & 0 & 0 \\ 0 & 0 & 0 & -0.0003154 \end{bmatrix}, D = \begin{bmatrix} 0 & 0 \\ 0 & 0 \\ 0 & 0 \end{bmatrix} \end{aligned} \tag{18}$$

where MC1 and MC2 are the variable gains which are updated in the adaptive MPC scheme as provided in the Algorithm (selection of the operating modes in the tertiary layer). ΔSOC is the change in SOCs between μGs due to $P_{\mu G1,2}$ and $P_{\mu G1,3}$. C_{SC}, C_{Bat}, and C_{Hyd} are the storage capacities of SC, battery, and hydrogen tank, respectively. $\zeta_{,}$ are the power conversion coefficients into equivalent energy content for the respective storage devices and are taken from [33]. *C* is storage capacity.

The objective cost-function in the MPC can be formulated as follows:

$$\begin{aligned} J = \sum_{j=1}^{\text{Nu}} & \alpha_1 {P_{\mu G1,2,\text{ref}(t+j)}}^2 + \alpha_2 {P_{\mu G1,3,\text{ref}(t+j)}}^2 \\ & + \beta_1 \Delta {P_{\mu G1,2,\text{ref}(t+j)}}^2 \\ & + \beta_2 \Delta {P_{\mu G1,3,\text{ref}(t+j)}}^2 \sum_{j=1}^{\text{Np}} \gamma_1 \Big(P_{O,\mu G1,2(t+j)} \\ & - P_{O,\mu G1,2,\text{ref}(t+j)} \Big)^2 \\ & + \gamma_2 \left(P_{O,\mu G1,3(t+j)} - P_{O,\mu G1,3,\text{ref}(t+j)}\right)^2 \\ & + \gamma_3 \left(\Delta\text{SOC}_{(t+j)} - \Delta\text{SOC}_{\text{ref}(t+j)}\right)^2. \end{aligned} \tag{19}$$

TABLE II

DETAILS OF THE PARAMETERS OF THE SECONDARY LAYER OF CONTROL

Parameters	Values
K_P, K_I	0.014, 0.8
$R_{t1,2}$, $L_{t1,2}$ (tie-line parameters among μGs)	0.2 (Ω), 50e–3 (H)
Off-grid inverter (full-bridge, LC filter type)	L_s=4e–4 H, C_s=4000e–6 (F), *f* (kHz)=2, R_o=100 (Ω)
t_{d1}, t_{d2}	*0.7 ms, 1 ms*

TABLE III

WEIGHT FACTORS IN MPC OPTIMIZATION OF TERTIARY LAYER

Parameters	Battery mode	FC mode
Weights		
α_1, α_2	0.1, 0.1	0.1, 0.1
β_1, β_2	0.1, 0.1	1, 1
γ_1, γ_2, γ_3	10, 10,0	10, 10,0
Output variables (OVs) min. ECR*	0, 0	0, 0
OV max. ECR	0, 0	0, 0
Manipulative variables (MVs) min. ECR	0, 0, 0, 0	0, 0, 0, 0
MV max. ECR	0, 0, 0, 0	0, 0, 0, 0
Constraints		
MV min. ($P_{\mu 1,2}$, $P_{\mu 1,3}$) W	–5000, –5000	–5000, –5000
MV max. ($P_{\mu 1,2}$, $P_{\mu 1,3}$) W	5000, 5000	5000, 5000
MV rate min. (Δ $P_{\mu 1,2}$, Δ $P_{\mu 1,3}$) W per sample	–2500, –2500	–0.01, –0.01
MV rate max. (Δ $P_{\mu 1,2}$, Δ $P_{\mu 1,3}$) W per sample	2500, 2500	0.01, 0.01
Measured output (MOs) min. ($P_{O,\mu G1,2}$, $P_{O,\mu G1,3}$) W	–5000, –5000	–5000, –5000
MOs max. ($P_{O,\mu G1,2}$, $P_{O,\mu G1,3}$) W	5000, 5000	5000, 5000
N_p, N_u, T_s (s)	20, 2, 100e^{-5}	20, 2, 100 e^{-5}

The first two weight terms (α) allow the relative utilization of manipulative variables. Weight factor β facilitates the weighted change in the manipulative variables. Weight factor γ is used for assigning the weight to the objectives. The values of the weight factors, physical constraints on manipulative variables, outputs, and rate constraints in (19) are provided in Table III. The ECR stands for the equal concern for relaxation. By opting for the appropriate value of ECR, the designer can provide reasonable flexibility at the constraints. For example, an ECR value equal to zero leads to hard constraints on associated parameters. In Table III, the battery and FC modes column denotes the weight factors used in (19) for the battery and FC operating modes, respectively.

B. *Secondary Layer of Control*

The objective of the secondary control layer is to control the power flow among the μGs. The reference power flow for the secondary control is generated by the tertiary control layer. The active power flow between two inverters can be represented as follows:

$$P = \frac{V_s V_r \sin\delta}{X} \tag{20}$$

$$Q = \frac{V_s V_r}{X} \cos \delta - \frac{{V_r}^2}{X} \tag{21}$$

where P and Q are active and reactive power, respectively. V_s and V_r are sending and receiving end voltages of inverters, respectively. X is the transmission line impedance, and δ is the phase angle difference between the sending and receiving ends. It is assumed that impedance is inductively dominated.

Hence, the power flow between the μGs can be controlled by controlling the phase angle between the μGs. The μGs are interconnected by each other using the VSIs. It is required that one μG inverter makes the reference grid, and the other μG inverters should follow it and change their phase angle relative to it (the reference grid inverter) as per the power requirement. Therefore, the VSI of μG1 makes the reference grid, and the VSIs of μG2 and μG3 follow this and change their phase angle.

Proportional–integral (PI) controller is used to obtain the value of the phase angle (Fig. 4). The value of the phase angle change can be obtained by

$$\delta_2 = (K_p + K_i/s)\left(P_{\mu G1,2(t+j)} - P_{\text{Ref,Net},\mu G1,\,2(t+j)}\right) \tag{22}$$

$$\delta_3 = (K_p + K_i/s)\left(P_{\mu G1,3(t+j)} - P_{\text{Ref,Net},\mu G1,\,3(t+j)}\right) \tag{23}$$

where k_p and k_i are the proportional and derivative gains of the PI controller (Table II). $P_{\mu G1,2(t+j)}$ and $P_{\text{ref},\text{Net},\mu G1,2(t+j)}$ represent the actual power exchange and reference power exchange between μG1 and μG2, respectively. Therefore, the reference voltage of the inverters can be formulated as follows:

$$V_{\text{VSI},\mu G1} = V_{\text{ref}} \sin(2\pi f_{\text{ref}})t \tag{24}$$

$$V_{\text{VSI},\mu G2} = V_{\text{ref}} \sin(2\pi f_{\text{ref}})t - \delta_2 \tag{25}$$

$$V_{\text{VSI},\mu G3} = V_{\text{ref}} \sin(2\pi f_{\text{ref}})t - \delta_3 \tag{26}$$

where V_{ref} and f_{ref} are the nominal values of the μG voltage and frequency, respectively. $V_{\text{VSI},\mu Gi\,=\,12,3}$ denotes the reference signals for the VSIs for μG1, μG2, and μG3, respectively.

The discrete state–space model of the VSI inverter can be represented as follows:

$$\begin{bmatrix} i_L\,(k+1) \\ V_o\,(k+1) \end{bmatrix} = \begin{bmatrix} 1 & -\frac{T_s}{L_s} \\ \frac{T_s}{C_s} & \left(1 - \frac{T_s}{R_o C_s}\right) \end{bmatrix} \begin{bmatrix} i_L \\ V_o \end{bmatrix} + \begin{bmatrix} \frac{T_s}{L_s} V_{\text{dc}} \\ 0 \end{bmatrix} u \tag{27}$$

where i_L and V_o are the inverter inductor current and output voltage, respectively; R_o, C_s, and L_s are the ac load resistance, output inverter capacitance, and inductance, respectively.

The cost function for the inverters can be given as follows:

$$J = \sum_{k=1}^{N_p} \lambda |V_{\text{VSI},\mu Gi=1,2,3}(t+k|t) - V_o(t+k)|^2 + \sum_{k=1}^{N_p} \beta |\Delta u(t+k-1)|^2 \tag{28}$$

where Δu and V_o are the control effort and output voltage of the inverter, respectively. The control effort is the magnitude of the sine wave which is compared with the triangular wave for generating the SPWM signal for the given inverters.

C. Primary Layer of Control

The objective of the primary control layer is optimally distributing the power among the components within each μG considering their response time and physical constraints on the SOCs. MPC methodology is used in the primary control layer. The state–space model for the primary layer can be provided as follows:

$$\begin{bmatrix} \dot{\text{SOC}}_{\text{SC}} \\ \dot{\text{SOC}}_{\text{Bat}} \\ \dot{\text{SOC}}_{\text{Hyd}} \end{bmatrix} = \begin{bmatrix} 1 & 0 & 0 \\ 0 & 1 & 0 \\ 0 & 0 & 1 \end{bmatrix} \begin{bmatrix} \text{SOC}_{\text{SC}} \\ \text{SOC}_{\text{Bat}} \\ \text{SOC}_{\text{Hyd}} \end{bmatrix} + \begin{bmatrix} \zeta_{\text{SC}} T_s / C_{\text{SC}} & 0 & 0 & 0 \\ 0 & \zeta_{\text{Bat}} T_s / C_{\text{Bat}} & 0 & 0 \\ 0 & 0 & \zeta_{\text{FC}} T_s / C_{\text{Hyd}} & 0 \end{bmatrix} \begin{bmatrix} P_{\text{SC}} \\ P_{\text{Bat}} \\ P_{\text{FC}} \\ P_{\text{Grid}} \end{bmatrix}. \tag{29}$$

The output matrix can be written as follows:

$$\begin{bmatrix} P_{\text{Net}} \\ \text{SOC}_{\text{SC}} \\ \text{SOC}_{\text{Bat}} \\ \text{SOC}_{\text{Hyd}} \end{bmatrix} = \begin{bmatrix} 0 & 0 & 0 \\ 1 & 0 & 0 \\ 0 & 1 & 0 \\ 0 & 0 & 1 \end{bmatrix} \begin{bmatrix} \text{SOC}_{\text{SC}} \\ \text{SOC}_{\text{Bat}} \\ \text{SOC}_{\text{Hyd}} \end{bmatrix} + \begin{bmatrix} 1 & 1 & 1 & 1 \\ 0 & 0 & 0 & 0 \\ 0 & 0 & 0 & 0 \\ 0 & 0 & 0 & 0 \end{bmatrix} \begin{bmatrix} P_{\text{SC}} \\ P_{\text{Bat}} \\ P_{\text{FC}} \\ P_{\text{Grid}} \end{bmatrix}. \tag{30}$$

C_{SC}, C_{Bat}, and C_{Hyd} are the storage capacities of SC, battery, and hydrogen tank, respectively. The cost function for the primary layer is given as follows:

$$\begin{aligned} J = \sum_{j=1}^{\text{Nu}} & \alpha_1 {P_{\text{SC}(t+j)}}^2 + \alpha_2 {P_{\text{Bat}(t+j)}}^2 + \alpha_3 {P_{\text{FC}(t+j)}}^2 \\ & + \alpha_4 {P_{\text{Grid}(t+j)}}^2 \quad + \beta_1 \Delta {P_{\text{SC}(t+j)}}^2 + \beta_2 \Delta {P_{\text{Bat}(t+j)}}^2 \\ & + \beta_3 \Delta {P_{\text{FC}(t+j)}}^2 + \beta_4 \Delta {P_{\text{Grid}(t+j)}}^2 \\ & + \sum_{j=1}^{\text{Np}} \gamma_1 \left(P_{\text{Net}(t+j)} - P_{\text{Net,ref}(t+j)}\right)^2 \\ & + \gamma_2 \left(\text{SOC}_{\text{SC}(t+j)} - \text{SOC}_{\text{SC,ref}(t+j)}\right)^2 \\ & + \gamma_3 \left(\text{SOC}_{\text{Bat}(t+j)} - \text{SOC}_{\text{Bat,ref}(t+j)}\right)^2 \\ & + \gamma_4 \left(\text{MHL}_{(t+j)} - \text{MHL}_{\text{Hyd,ref}(t+j)}\right)^2. \end{aligned} \tag{31}$$

The methodology and constants in (29) of the primary control layer and the weight-tuning and constraints of (31) are taken from [33]. This part is not discussed here in detail to avoid redundancy.

Information exchange is required among different layers in the μG groups. In practical applications, this information exchange

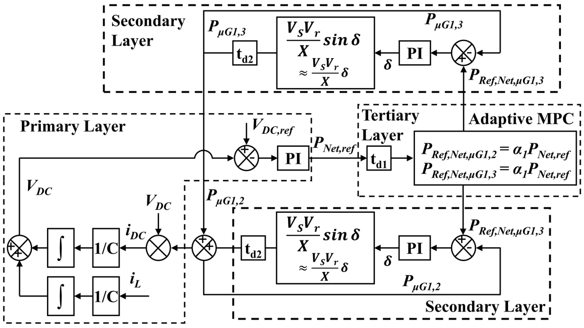

Fig. 7. Simplified overall control diagram of all layers.

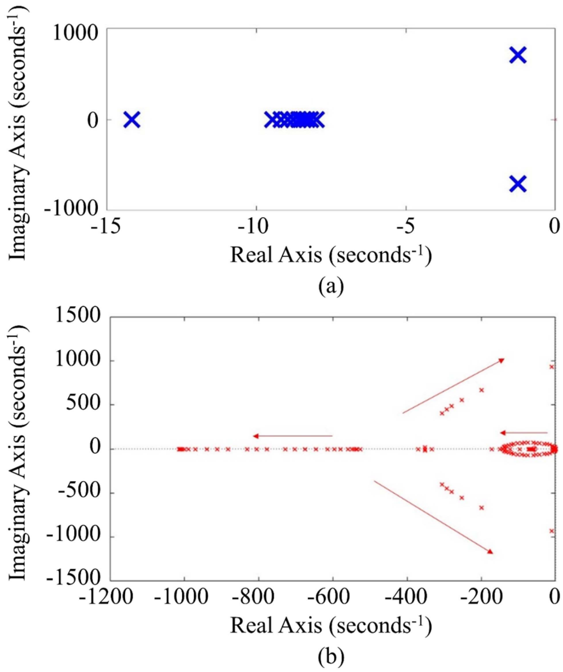

Fig. 8. Stability analysis of the system: (a) secondary layer and (b) overall system.

can be achieved via wired (i.e., PLC or CAN) or wireless (i.e., Zigbee, Wi-Fi, Bluetooth, or cellular network communication) [36]. In this article, the direct connection of different signals is considered for information exchange in simulation development.

The overall stability of the overall system (primary, secondary, and tertiary) is studied in a simplified scenario. In this cluster of μGs, the power exchange occurs when all the storages are saturated and power balance is achieved by exporting/importing the power to other μGs. Therefore, during the power exchange among the μG, the dc bus voltage is regulated by exchanging power with other μGs and the overall system can be simplified as shown in Fig. 7. Furthermore, it is assumed the MPC controller in the second and tertiary layer is sufficiently fast to track the reference value. A delay is added in the control loops to take care of the delay in tracking the reference values in MPC controllers. The secondary layer MPC stability is studied as shown in Fig. 8(a). The Root locus diagram shows that for the giving tuning parameters (weight factors) the system behaves stably. Similarly, using the design parameters the overall system behaves stable as shown in Fig. 8(b).

D. Design Guidelines and Procedure for the Proposed Controller

The tertiary layer working is based on the optimization of the cost-function J. MPC optimizes its control actions (manipulative variables) to minimize the cost-function subjected to given constraints on the control and output variables. By using the appropriate weights, one manipulative variable can be penalized compared to another in optimization. Therefore, tuning of parameters is essential for the desired response of the controller. In the tertiary layer of control, tracking the reference power is of utmost importance; therefore, high values are assigned to $\gamma 1$ and γ_2. However, the minimization of the SOC difference between the ESSs in μG 2 and μG 3 is not important; therefore, γ_3 is kept at 0 to provide flexibility in the operation. For effective power balance, the cost terms associated with $P_{\mu G1,2}$ and $P_{\mu G1,3,}$ and $\Delta P_{\mu G1,\,2}$ and $\Delta P_{\mu G1,\,3}$are relatively less important compared to tracking the power reference signal. Therefore, in battery mode (Table III), lower weights are assigned to β_1 and β_2 as compared to the Υ_1 *and* Υ_2. Similarly, lower values of α_1 and α_2 are assigned as compared to Υ_1 and Υ_2. However, the FC mode has higher weights of β_1 and β_2 for penalizing the rate of power exchange during this mode. In addition, further constraints are added to the rate of power change during FC mode. In this case, it was kept at 100 W/s.

Prediction and control horizons are also very important in the controller design. Generally, a suitable choice can be $T = T_s N_p$, where N_p is the prediction horizon, T_s is the sampling time, and T is the desired response time. The control horizon (N_c) must be equal to or less than the prediction horizon. A large value of the control horizon may require a high computational power. In the present article, several simulations in different conditions were performed for the suitable choice for N_P and N_c.

Similarly, in case of designing the MPC for the secondary layer to minimize the cost function (28), tracking the reference output voltage is of utmost importance. Therefore, the higher weight is assigned to λ (for tracking reference signal) while the lower weight is assigned to β (for control move).

The power-sharing among the μGs depends on the SOC and MHL of ESSs in the given cluster. This accurate power-sharing can be achieved by updating the parameters MC1 and MC2 using adaptive MPC (refer to selection of the operating modes in the tertiary layer algorithm). MC1 and MC2 can be defined as variables that depend on the SOCs and MHLs of μGs. The calculation of these variables is conducted based on certain decision-making using the algorithm (selection of the operating modes in the tertiary layer) in Fig. 6. Therefore, MC1 and MC2 are estimated based on the SOC and MHL values in mode 1, mode 2, and mode 5. In mode 1 and mode 2, power-sharing is based on the SOCs of ESSs and in mode 5 power-sharing is based on the MHLs. However, in certain situations, SOC or MHL-based power-sharing among μGs is not desirable. For example, SOC in μG 2 is out of the working range while SOC in μG 3 is in the working range. Therefore, in such a

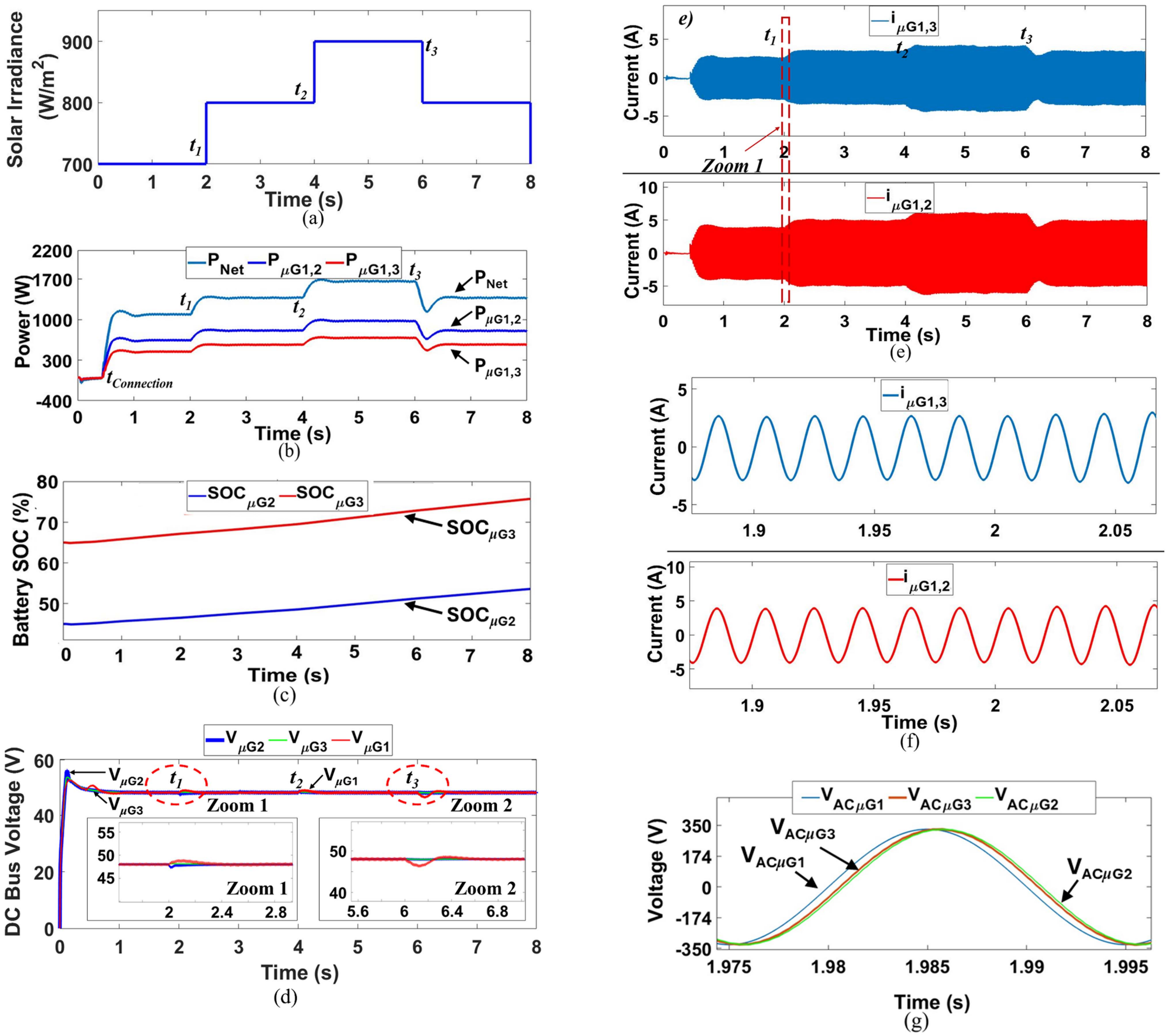

Fig. 9. Coordination of proposed controller for μGs cluster in Scenario 1. (a) Solar Irradiance. (b) Power exchange among the μGs. (c) SOCs in μGs. (d) DC bus voltage in the μGs. (e) Current exchange among the μGs. (f) Current exchange among the μGs zoomed-in view. (g) AC bus voltage in the μGs.

situation, FC power in μG 2 can be used for power exchange among μGs avoiding the overcharging and deep-discharging of the battery. However, utilization of the FC in μG 2 is not as energy efficient as compared to the battery. Hence, the proposed controller prefers to share the entire power with μG 3 which has a battery SOC in the working range. By doing this, both objectives of energy-efficient operation (avoiding the FC operation) as well as avoidance of the deep-discharging and overcharging of the battery storage can be achieved. In other words, the proportional power-sharing is disabled and power is exchanged between two μGs only (that SOC in the working range). In such cases, MC1 and MC2 are chosen appropriately. The high weight of MC is used to minimize the power exchange with the associated μG. For example, in mode 4, μG 2 does not have SOC in the working range while μG 3 has SOC in the working range; therefore, as per control logic it is intended to exchange the power between μGs 1 and 3 and power exchange between μGs 1 and 2 should be disabled. This is achieved using a high value of MC1 which is taken around 200 and a low value of MC2 which is 1 (refer to mode 4 in selection of the operating modes in the tertiary layer algorithm). Selection of the operating modes in the tertiary layer). Using value 1 for MC2 ensures that all the power is exchanged between μGs 1 and 3. Similarly, MC1 and MC2 are updated for mode 4, mode 6, and mode 7.

The adaptive MPC accurately updates the plant matrices by measuring the SOC and MHL in real-time conditions. Therefore, accurate power-sharing among the μGs can be ensured based on the SOC/MHL. The power exchange among the μGs during the FC mode (when hydrogen MHL is within the range) is effectively controlled by incorporating the constraints on the maximum and minimum values of the rate of power exchange. In addition, the appropriate weights of the rate of power exchange (as given in Table III) are also chosen carefully. During smooth power control of power exchange among μGs, grid power is used to provide the required power balance in the μG cluster. In this mode, power exchange among the μGs (provided by

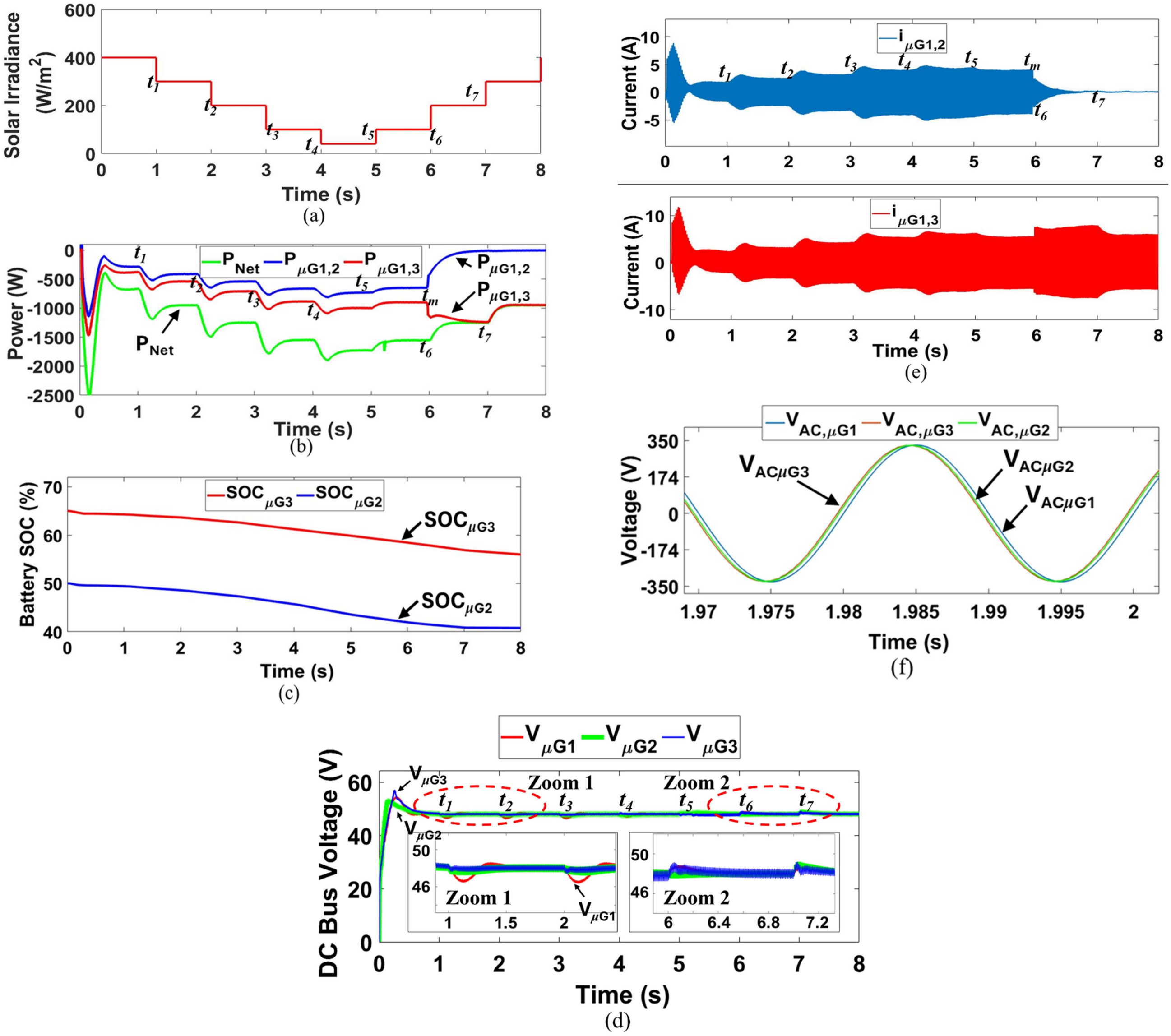

Fig. 10. Coordination of the proposed controller for μGs cluster in Scenario 2. (a) Solar Irradiance. (b) Power exchange among the μGs. (c) SOCs in μGs. (d) DC bus voltage in the μGs. (e) Current exchange among the μGs. (f) AC bus voltage in the μGs.

the FC generators) is smoothly controlled by the tertiary layer ensuring the better and more durable operation of the FCs. A similar approach is used for the battery mode, however, a less strict condition is imposed for the rate of power exchange during battery mode as compared to the FC mode (Table III). Effective and controlled power exchange using tertiary layer control provides efficient and durable operation of the FC. The tuning of the PI in table is performed by the root locus method by obtaining the transfer function of (22)–(24).

IV. RESULTS AND DISCUSSIONS

A. *Scenario 1: μG1 Has Surplus Power and Battery Storage in μG2, and μG3 is in the Functional Range (40%–80%)*

The working of the unified controller in Scenario 1 is shown in Fig. 9. In this scenario, both μG2 and μG3 have battery SOC in the working range corresponding to mode 2 (selection of the operating modes in the tertiary layer algorithm). The status of the $P_{\mathrm{Net,ref}}$ in the μG1 is negative (the sign convention has been taken reverse as compared to algorithm [selection of the operating modes in the tertiary layer, in Fig. 9(b) for better illustration]. Battery SOC in μG1 reaches the maximum value (approximately 78%), which means that an excess of power needs to be utilized to maintain the power balance in the μG1. The power imbalance in the μG1 is simulated by varying PV power, as shown in Fig. 9(a) at instants t_1, t_2, and t_3, respectively. Fig. 9(b) shows that as the power imbalance in μG1 happens, the power exchange among the μGs is varied proportionally. Fig. 9(b) represents the power distribution $P_{\mu G1,2}$, and $P_{\mu G1,3}$ which is proportional to the SOC of μG2 and μG3. The SOC of the μG3 is higher than the SOC of μG2; therefore, the magnitude of the power flow $P_{\mu G1,2}$ is higher than the power flow between $P_{\mu G1,3}$, which is consistent with the derived equations in (5), (6), and (7). As the power exchange between the μGs is used to charge the battery storages in respective μGs, the SOCs of battery storage in μG2 and μG3 increase correspondingly, as justified in Fig. 9(c). The stability of the dc bus voltage in different μGs is shown in Fig. 9(d). The transient variations in the dc bus voltage in μG1 correspond to the transient power imbalance. In Fig. 9(e), the magnitude of the current flowing $i_{\mu G1,2}$ and $i_{\mu G1,3}$ between the μGs is proportional to the corresponding values of the power exchange $P_{\mu G1,2}$ and $P_{\mu G1,3}$, respectively. This can be seen as the proposed unified control facilitates the stable operation of all the μGs during all the conditions of the power imbalances. The waveforms of the ac current flowing between the different μGs are shown in Fig. 9(e). Fig. 9(f) shows the zoom-in view of ac current waveforms in the tie-lines among the different μGs. The output voltage waveforms of the VSIs in different μGs are shown in Fig. 9(g). Based on the power reference signals generated by the tertiary layer control, the secondary layer control adjusts the relative phase angles of the respective VSIs. The VSI in the μG1 (VSI$_{\mu\mathrm{G1}}$) functions as a reference voltage node while the magnitude and phase of the VSIs in μG2 and μG3 (VSI$_{\mu\mathrm{G2}}$ and VSI$_{\mu\mathrm{G3}}$) are adjusted according to the VSI$_{\mu\mathrm{G1}}$. The phase of the VSI$_{\mu\mathrm{G2}}$ and VSI$_{\mu\mathrm{G3}}$ are lagged compared to the VSI$_{\mu\mathrm{G1}}$ depending on the power exported from the μG1 to μG2 and μG1 to μG3. As the power exchange $P_{\mu G1,2}$ is higher compared to $P_{\mu G1,3}$, the phase difference between $V_{AC\mu G1}$ and $V_{AC\mu G2}$ is greater than that between the $V_{AC\mu G1}$ and $V_{AC\mu G3}$. It is worth mentioning that small capacities of ESS are used for showing reasonable variations in the SOC and MHL in a short time duration.

B. Scenario 2: μG1 Has Deficit Power and Battery Storage in μG2, and μG3 is in the Functional Range (40%–80%)

The working of the unified controller in Scenario 2 is shown in Fig. 10. In this scenario, the battery SOCs in μG2 and μG3 are in the working range; however, power is in deficit (mode 1, selection of the operating modes in the tertiary layer algorithm). Therefore, to maintain the power balance in the μG1, deficit power needs to be imported from the μG2 and μG3. Fig. 10(a) shows the transient power imbalance due to variation in solar irradiance at the instants t_1, t_2, t_3, t_4, t_5, and t_6, respectively. The power exchange at these instants is shown in Fig. 10(b). The magnitude of the power is negative which shows the power is imported from μG2 and μG3 to μG1 [the sign convention has been taken reverse as compared to algorithm; selection of the operating modes in the tertiary layer in Fig. 10(b) for better illustration]. The power exchange is inversely proportional to the PV power because lower PV output requires more power to be imported from the other μGs to balance the supply and demand in the μGs cluster. The value of the SOC in μG3 is higher compared to that in the μG2; therefore, power flow $P_{\mu G1,3}$ is higher compared to the $P_{\mu G1,2}$, which is in accordance with (2), (3), and (4). The SOC values decrease in the respective μGs, as shown in Fig. 10(c), which is justified by the discharge of battery storages in μG2 and μG3. The stability of the dc bus in the μGs cluster is shown in Fig. 10(d). It represents the transient variation in the dc bus voltage of μG1 due to power imbalance [Fig. 10(d)]. It can be seen that the dc bus remains stable in all the instants of the power transients. The waveforms of the ac current in the tie-lines between μG1,2 and μG1,3 are shown in Fig. 10(e). The magnitude of the current following $i_{\mu G1,2}$ and $i_{\mu G1,3}$ between the μGs is proportional to the power exchange $P_{\mu G1,2}$ and $P_{\mu G1,3}$, respectively, as shown in Fig. 10(e).

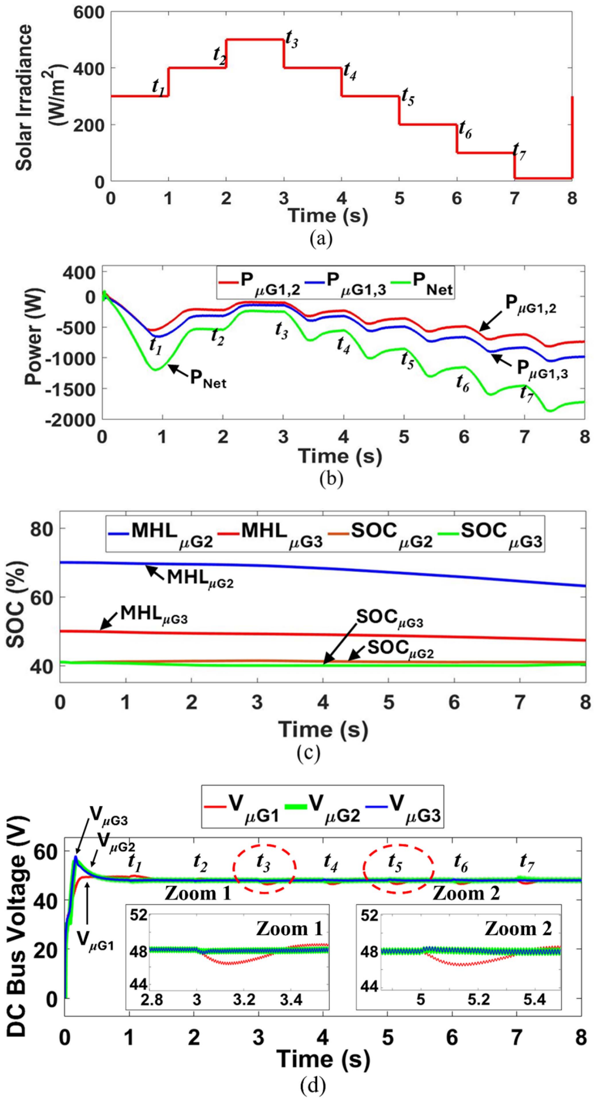

Fig. 11. Coordination of the proposed controller for μGs cluster in Scenario 3. (a) Solar Irradiance. (b) Power exchange among the μGs. (c) SOCs and MHLs in μGs. (d) DC bus voltage in the μGs.

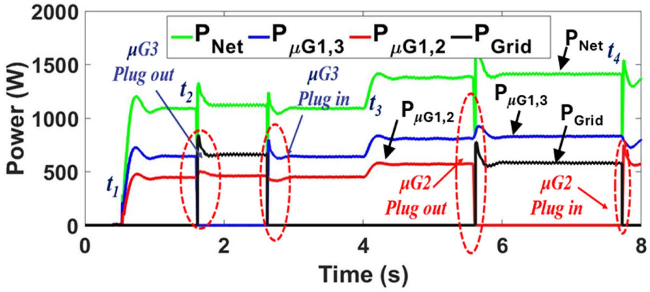

Fig. 12. Plug and play performance of μGs cluster.

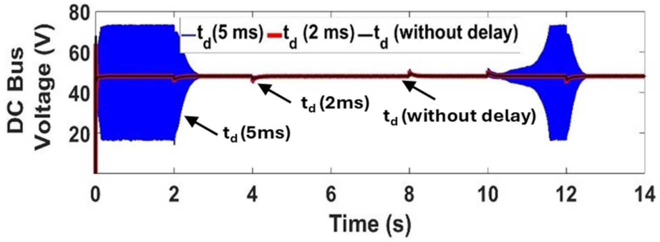

Fig. 13. Effect of the time delay on the DC-link voltage.

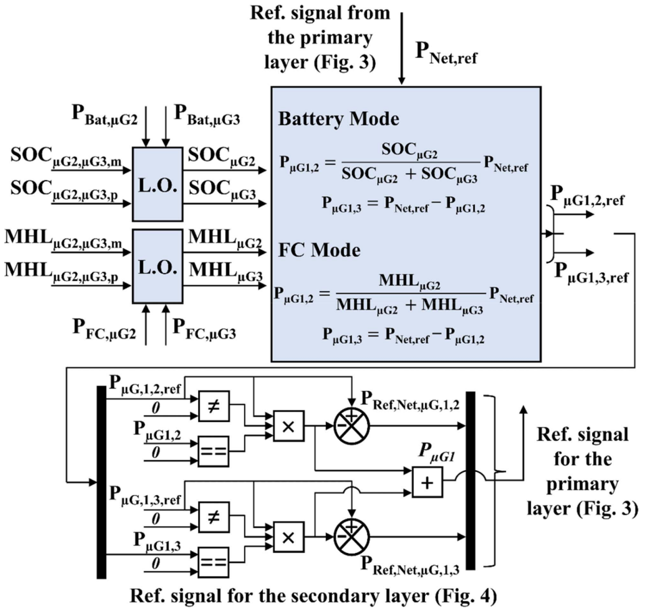

Fig. 14. Rule-based proportional power sharing based tertiary layer control (Conventional 1).

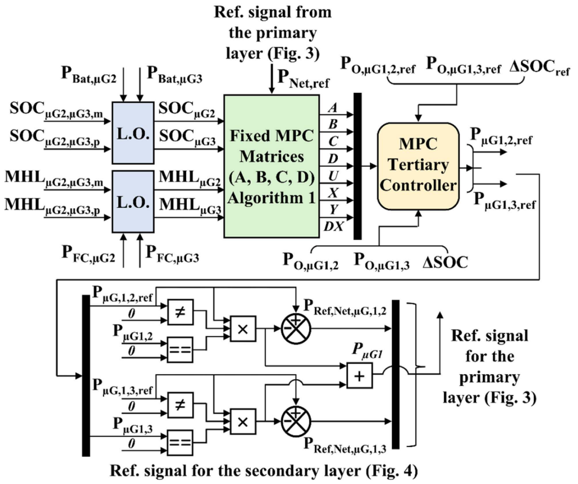

Fig. 15. Without adaptive MPC-based proportional power sharing based tertiary layer control (Conventional 2).

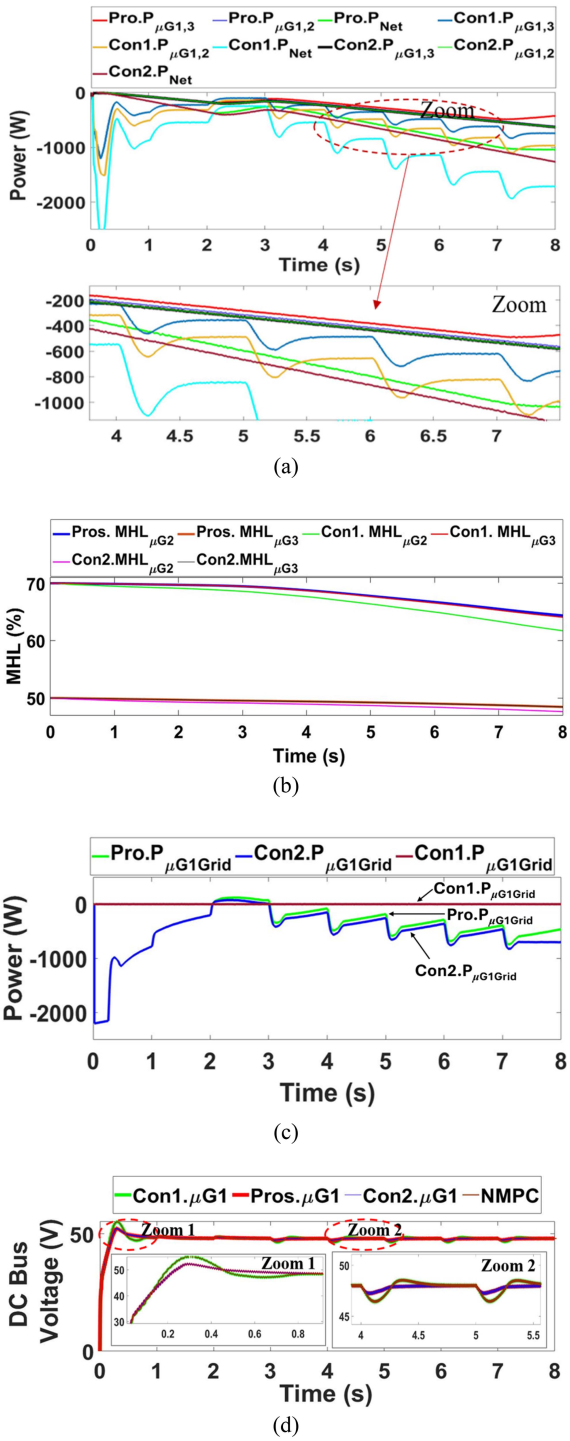

(a)

(b)

(c)

(d)

Fig. 16. Comparison of power distribution using different control approaches. (a) Power exchange among the μGs. (b) SOCs and MHLs in μGs. (c) Power exchange with grid. (d) DC bus voltage in the μGs.

The zoomed-in view of the waveforms of the VSIs in all three μGs at a given instant is provided in Fig. 10(f). Following the power reference signals by the tertiary layer control, the secondary layer controls the relative phase angles of the respective VSIs. As it can be seen that the power is imported to the μG1 from μG2 and μG3; therefore, the phase of $\mathrm{VSI}_{\mu G1}$ lagged compared to the $\mathrm{VSI}_{\mu G2}$ and $\mathrm{VSI}_{\mu G3}$. As the power exchange $P_{\mu G1,2}$ is lower compared to $P_{\mu G1,3}$, the phase difference between $V_{\mathrm{ac},\mu G1}$ and $V_{\mathrm{ac},\mu G3}$ is higher (lagging) than that between $V_{\mathrm{ac},\mu G1}$ and $V_{\mathrm{ac},\mu G2}$. Fig. 10(b) instant t_m, represents the transition from mode 1 to mode 7 (selection of the operating modes in the tertiary layer algorithm). In this case (mode 7), the

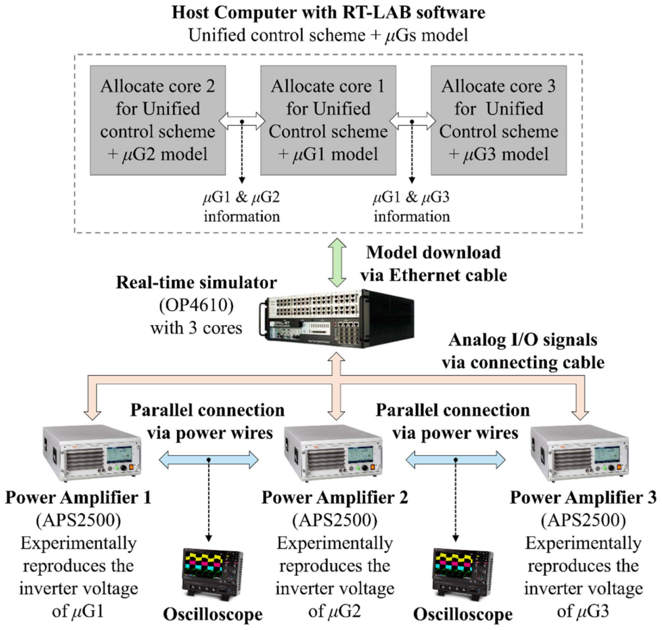

Fig. 17. Schematic of the PHIL experimental setup.

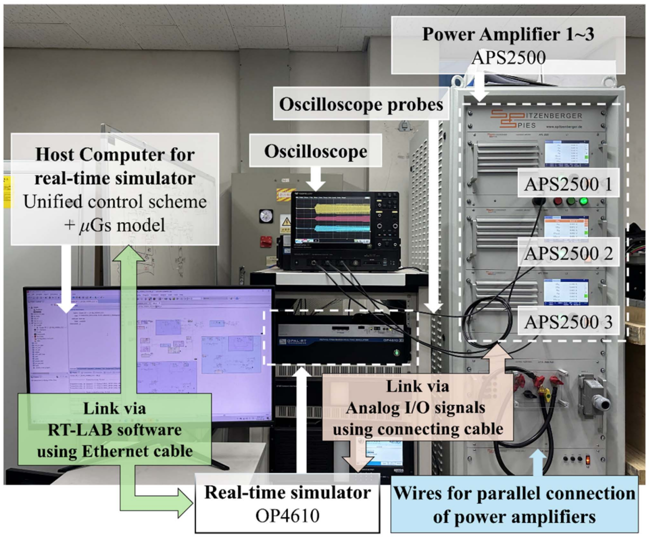

Fig. 18. PHIL experimental setup.

power exchange occurs only between μG 1 and 3, and $P_{\mu G1,2}$ decreases to zero because the SOC of the μG3 decreases to a lower value (nearly 40%). This is achieved by assigning a higher value in MC1 as compared to MC2 in the selection of the operating modes in the tertiary layer algorithm.

C. Scenario 3: μG1 Has Deficit Power, and Hydrogen Storage is in the Functional Range in μG2 and μG3 (20%–90%)

In this scenario, the hydrogen storage in μG2 and μG3 is active, which means both SOCs of battery storage in μG2 and μG3 have achieved lower limits of SOC. Therefore, the deficit power in μG1 needs to be provided by the FCs from the μG2 and μG3. In this case, the magnitude of the power exchange among the μGs is inversely proportional to the PV power because a lower value of PV power needs more power to be imported to make the balance in supply and demand. This power exchange is made by the FCs of respective μGs; therefore, the corresponding values of the MHL in μG2 and μG3 decrease, as shown in Fig. 11(c). The SOC values in μG2 and μG3 remain stable as they are dormant and do not operate in this scenario [Fig. 11(c)].

TABLE IV
THD Performance of the VSI in a Given Microgrid Cluster

	Inverter voltage THD (%) for *β=0.01 tuning weight in (28)*		
N_p	N_u=1	N_u=2	N_u=3
2	3.1	3.12	3.11
4	2.89	2.81	2.82
6	2.81	2.81	2.81
8	2.6	2.5	2.5
10	2.5	2.4	2.4
15	2.6	2.7	2.8
20	2.7	2.7	2.9

As FC has a slow response, the power output of the FC varied in a controlled way as mentioned in Table III. The different weight factors and constraints are used in the case of FC mode.

As the value of the MHL in μG2 is higher as compared to that in μG3, power flow $P_{\mu G1,2}$ is higher as compared to $P_{\mu G1,3}$, which is in good agreement with the design formulation in Section III-A (8), (9), and (10). The power curve in this scenario is shown in Fig. 11(b), while the status of MHLs is shown in Fig. 11(c). Fig. 11(d) depicts the transient variations in the dc bus voltage of the μG1 during the power imbalance conditions which is justified.

D. Performance Analysis of the Proposed Controller for Voltage Source Inverter and DC–DC Converter

As a case study (Scenario 1) in a given μGs cluster, it is found that the proposed method decreases the inverter voltage THD and rms error by 23.04% and 34.87%, respectively, compared to the conventional PID-based method. In the given microgrid cluster, the THD of the VSI inverter current and grid current are found to be 3.85% and 3.24%, respectively. The MPC is applied to track the reference inductor current of the dc–dc converter in the primary layer of the μGs cluster; it is found that maximum overshoot decreases by 5.23% and the setting time reduces to 1 from 10 ms compared to the conventional PI method. A comparative study is performed in the present article to evaluate the performance of PI-MPC and deadbeat-MPC in the secondary layer and their effect on the system performance. It is found that the dc bus overshoot increases by 1.2% in deadbeat MPC as compared to the proposed PI-MPC. However, the setting time decreased to 0.85% in the deadbeat MPC as compared to the proposed method. Table IV shows the THD at the output voltage of the inverter for different values of the prediction and control horizons. It is found that the THD value does not vary significantly by increasing the control horizon; however, it increases the computational requirements. THD value increases for the lower and higher values of the prediction horizon. For example, Table IV shows that the THD value is higher for $N_p = 2$ and reduced for $N_p = 10$. Therefore, there is a tradeoff between the accuracy and computational requirement, and a suitable value

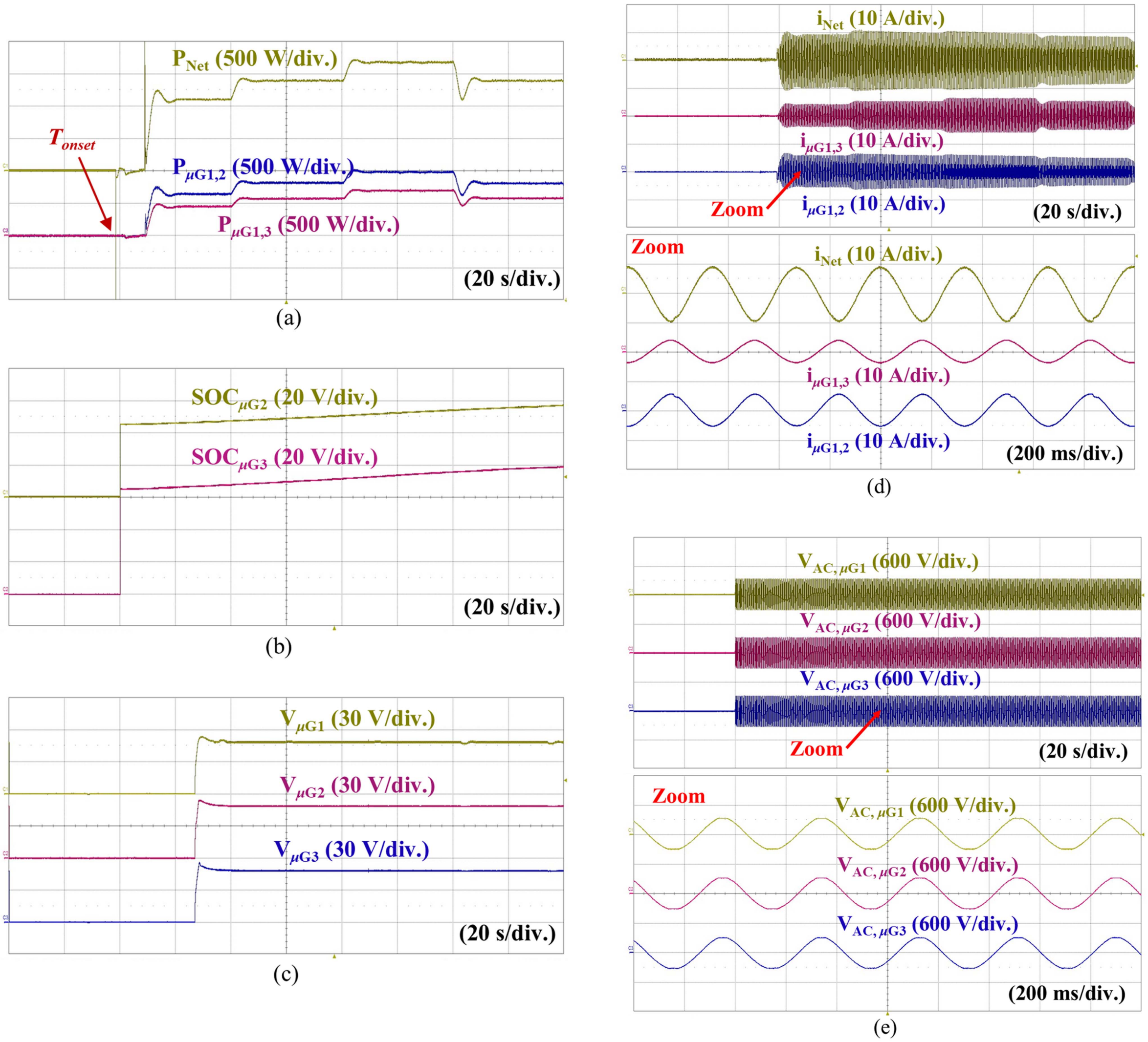

(a) (b) (c) (d) (e)

Fig. 19. PHIL analysis of the proposed controller in Scenario 1. (a) Power exchange among the μGs. (b) SOCs in μGs. (c) DC bus voltage in the μGs. (d) Current exchange among the μGs. (e) AC bus voltage in the μGs.

TABLE V
RMS ERROR ANALYSIS OF THE VSI IN A GIVEN MICROGRID CLUSTER

	Inverter voltage rms error (%) for *β=0.01 tuning weight in (28)*		
N_p	$N_u=1$	$N_u=2$	$N_u=3$
2	0.47	0.46	0.46
4	0.46	0.46	0.46
6	0.44	0.43	0.42
8	0.42	0.42	0.42
10	0.41	0.40	0.40
15	0.43	0.42	0.42
20	0.45	0.45	0.45

of the prediction and control horizon is selected considering the required accuracy and computational requirement. Table V shows the rms error at the inverter output for different values of the control and prediction horizons.

A parametric uncertainty analysis is performed for the inverter system using the adaptive MPC in the present article, to evaluate the robustness of the proposed MPC controller for the inverter system. *LC* parameters uncertainty can happen in the inverter system due to temperature effects and aging of components. Multiple simulations have been carried out to evaluate the *LC* parameter uncertainty on the grid power. In the simulation, the plant model of the voltage source converter is kept similar, while the values of the *LC* filter parameters in the physical circuit are varied. The effect of the *LC* parameters on the inverter current is analyzed. It is found that the present controller is robust against the reasonable uncertainty in the *LC* parameters (−60% to 80%). It is found that the inverter current remains stable and its THD varies from 4.2% to 4.8% for −60% to 80% variation in the uncertainty in *L* and *C* values of the inverter system. The inverter current THD is 3.24% at the original values of the *L* and *C* (considering negligible uncertainty) in the inverter system. The adaptive MPC-based tertiary layer also handles the uncertainties in hybrid storage's SOC and facilitates the desired power sharing.

μG 1 is connected to the main grid using the grid-connected inverter. This grid-connected inverter is controlled using the MPC controller. The MPC for the inverter enables the robust performance of the inverter during the changes in the grid

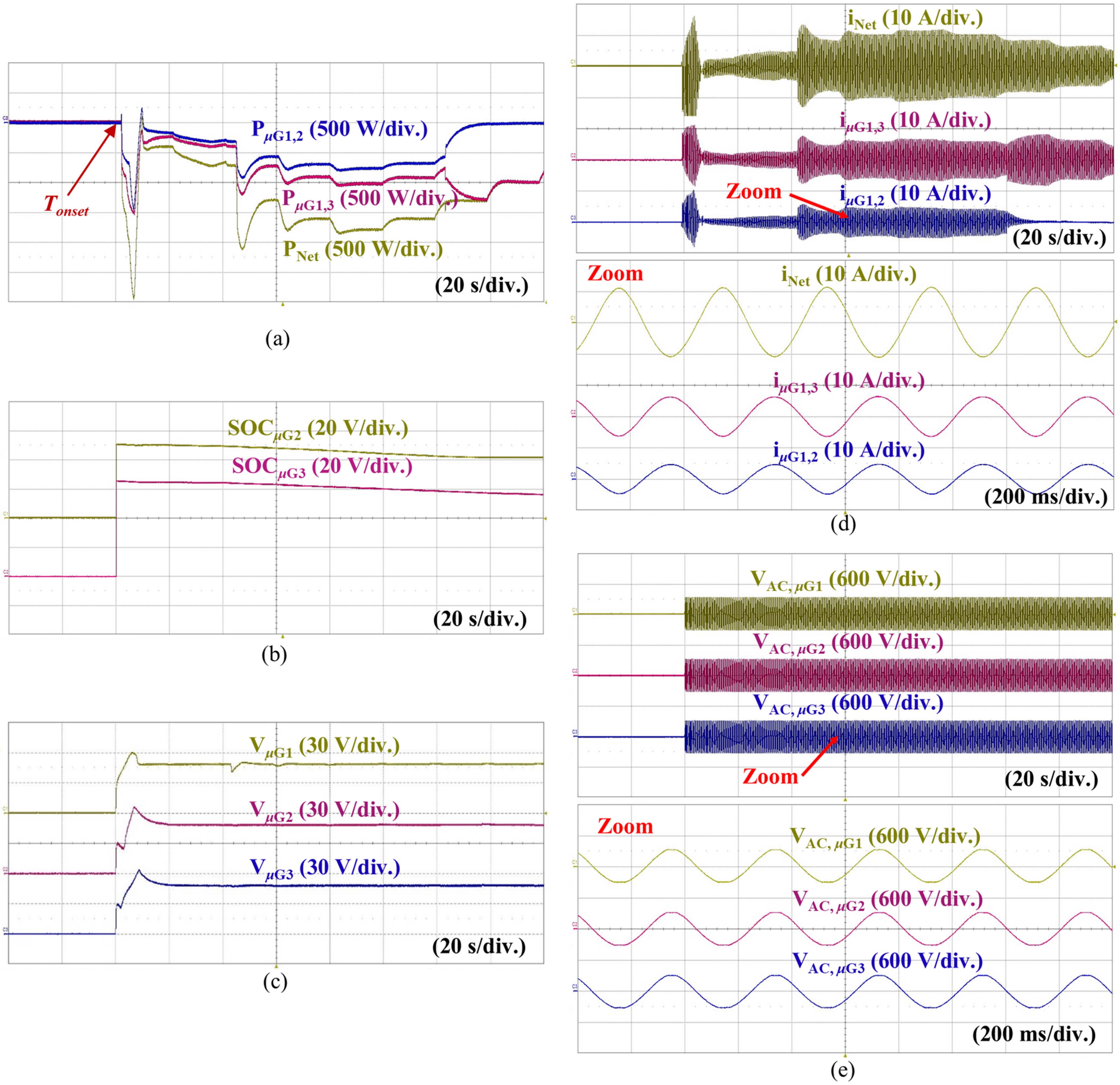

(a) (b) (c) (d) (e)

Fig. 20. PHIL analysis of the proposed controller in Scenario 2. (a) Power exchange among the μGs. (b) SOCs in μGs. (c) DC bus voltage in μGs. (d) Current exchange among the μGs. (e) AC bus voltage in the μGs.

conditions such as variation in the grid frequency and voltage. It is found that the power exchange with the grid remains stable concerning the 0.5% and 5% variations in the grid frequency and amplitude of the grid voltage, respectively.

E. Plug-and-Play of μGs

The plug-and-play performance of the proposed controller is validated in this section. The μG1 and μG2 are disconnected and reconnected at certain instants (t_1, t_2) and (t_3, t_4), respectively, as shown in Fig. 12. The operation of the μG remains stable and power balance is achieved. During the events of disconnection of the μG2 and μG3, the surplus power is supplied to the grid to provide the balance in the supply and demand in the μGs cluster. As soon as given μG1 or μG2 is reconnected to the μG1, the grid power becomes zero. Therefore, it is concluded that the proposed unified controller is fully capable of handling the plug-and-play characteristics of the μGs.

F. Effect of Time Delay

The effect of the delay in the tertiary layer on the overall system stability was observed. It was found that the proposed control scheme worked satisfactorily for a considerable range of the delay and the dc bus for μG1 remained stable showing stable behavior of the overall system. However, for a large value of the delay the dc bus voltage started showing unstable behavior as shown in Fig. 13.

G. Comparison With Existing Benchmark Methods

The proposed power-sharing scheme has been compared with existing/conventional methods [1], [17]. In conventional 1 (Con1), the power-sharing among μGs is achieved by a

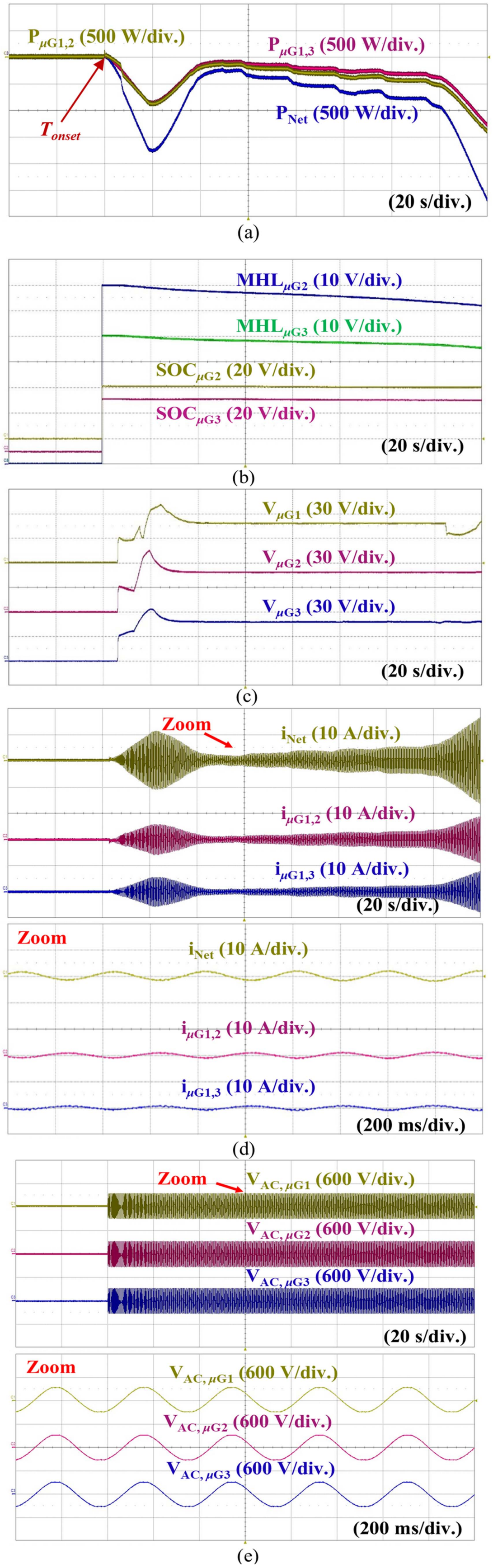

Fig. 21. PHIL analysis of the proposed controller in Scenario 3. (a) Power exchange among the μGs. (b) SOCs and MHLs in μGs. (c) DC bus voltage in μGs. (d) Current exchange among the μGs. (e) AC bus voltage in the μGs.

TABLE VI
COMPREHENSIVE ANALYSIS OF DIFFERENT CONTROL STRATEGIES

Parameters	Con 1	Con 2	NMPC	Proposed
Max. $\Delta P_{\mu G,1,2}$ (W/s)	6693	100	110	100
Max. $\Delta P_{\mu G,1,3}$ (W/s)	7246	100	100	100
Min. $\Delta P_{\mu G,1,3}$ (W/s)	−5215	−100	−115	−100
Min $\Delta P_{\mu G,1,3}$ (W/s)	−3728	−100	−100	−100
ΔMHL (%)	5.91	4.34	5.70	4.05
Max. dc bus voltage (V)	1.67	0.91	1.62	0.92
Max. overshoot dc bus (%)	15.02	9.02	14.88	9.02

rule-based approach as shown in Fig. 14. The conventional 2 (Con2) strategy does not use adaptive MPC features in power sharing as shown in Fig. 15. The proposed adaptive MPC is suitable for handling the constraints on the rate of power exchange among μGs. Therefore, a smooth variation in the power exchange among μGs can be ensured during the FC operations using the proposed tertiary control as shown in Fig. 16. This is very helpful for the durability improvement of the FC device whose lifespan can be adversely affected by the high-frequency operating power. It is worth mentioning that the rate of power exchange among μGs is strictly regulated [using high weight factors in (19) compared to Scenario 3]. Conventional 1 is ineffective for conventional 2 facilitates equal power-sharing irrespective of the SOC. The difference in MHL for different μGs is shown in Fig. 16(b). The difference in the MHL between μG2 and μG3 can be reduced significantly using the proposed method compared to the conventional 2. However, a higher value of difference in the MHL is obtained using the conventional 1 power scheme. This can be due to the high-power output of FC in both μGs. However, this uncontrolled FC output is not desirable for FC considering its slow response and tendency to performance decline at high fluctuating power. Therefore, the proposed method is more effective considering the controlled (smooth) power exchange as well as minimizing the difference in the MHL between μGs. The effect of the dc bus regulation using the proposed and conventional methods is shown in Fig. 16(d). It can be seen that the proposed method is effective in minimizing the maximum overshoot in the dc bus as compared to conventional 1. A comprehensive comparison of the performance of μGs in different cases is provided in Table VI. In the present article, the steady-state error for tracking the reference dc bus voltage of microgrids with the complete MPC-based model was found to be 0.41% while the PI-MPC-based method was found to be 0.19%. The results demonstrate that the rate of power change is effectively controlled in the proposed method compared to the conventional 1. The zoom-in-view of the power exchange is shown in Fig. 16(a). Fig. 16(d) shows the comparison of power exchange with the grid for different control strategies. In the proposed method, the rate of change of FC power is controlled and restricted, resulting in higher power exchange with the grid in both the proposed and conventional 2 methods compared to conventional 1. The maximum overshoot in the dc bus in μG1 decreases by 39.94% while the maximum deviation in the dc bus is reduced by 42.44% using the proposed method as compared to the conventional 1. Table VI provides a comprehensive comparison between the proposed method and existing benchmarks.

One of the major advantages of the proposed method is that the difference between the SOC of the hybrid ESS for μGs can be minimized. As the level of the SOC of hybrid ESS (for given storage for example battery or hydrogen) given μG indicates the level of surplus renewable energy; therefore, the SOC-based power-sharing equalizes the level of surplus/deficit renewable power. In addition, the tertiary layer also provides energy-efficient operation by enabling the higher power exchange with μG having battery SOC in the working range as compared to other μG (where hydrogen storage is working). The proposed method also considers the rate of power change of the expensive devices i.e., FC which is helpful for the betterment of their lifespan. The MPC is also helpful for operating the hybrid ESS in a safe operating range of SOC; which is better for their safe and reliable operation. The proposed tertiary controller also enables the smooth plug-in and plug-out operation of the μGs.

H. Experimental Analysis

For experimental verification, the proposed controller is implemented using PHIL equipment, with the real-time simulator OPAL-RT4610 and the power amplifier APS2500. The μGs cluster model is designed on the host computer using MATLAB 2018 and executed on the target computer via the RT-Lab tool. The RT-Lab interface generates the C code of the plant model and compiles it on the CPU of the host computer. The description of the PHIL experimental setup is depicted in Figs. 17 and 18. One core is used for replicating each μG; therefore, a total of three cores are used. The inverters' voltage, current, and power as well as the μGs' connection points are replicated by three power amplifiers (APS2500 1–3) connected in parallel as shown in Fig. 18. In other words, the voltage and current of the VSI located in each μG are reproduced through each power amplifier. In detail, the inverter voltage and current of μG1 are reproduced through power amplifier 1, which operates in constant voltage mode to perform voltage control on the voltage of the μG interconnection point. The inverter voltage and current of μG2 are reproduced through power amplifier 2, which operates in constant current (CC) mode to perform current control on the current input and output through μG2. Similarly, the inverter voltage and current of μG3 are reproduced through power amplifier 3, which operates in CC mode to replicate the current amount of μG3. As a result, since the power amplifiers are connected in parallel, the currents flowing into (or going out from) μG2 and μG3 are combined and output from power amplifier 1. The combined quantity current is fed into the real-time simulator device (OP4610) through the analog input port.

Experimental verification using PHIL is performed based on the three scenarios applied in the simulation verification. The experimental verification results are measured from the (T_{onset}) to the scenario end time using an oscilloscope. Fig. 19 shows the experimental validation results of the proposed controller in Scenario 1 using PHIL. As can be seen, the power exchange between the μGs is proportional to the SOCs of the storage. The variations in SOCs of the respective μGs are shown in Fig. 19(b). The 20 V in Fig. 19(b) in SOC represents 20% of SOC. The variations in the dc bus voltages of the given μGs are demonstrated in Fig. 19(c) using the PHIL experiments. The dc bus voltages of μG1 ($\text{V}_{\mu\text{G1}}$), μG2 ($\text{V}_{\mu\text{G2}}$), and μG3 ($\text{V}_{\mu\text{G3}}$) are shown to remain stable under all power imbalance conditions through the proposed unified control. Fig. 19(d) depicts the flowing of the ac current exchange among the μGs. As designed in the PHIL experimental setup, the current exchange between μG1 and μG2 ($i_{\mu\text{G1,2}}$) and the current exchange between μG1 and μG3 ($i_{\mu\text{G1,3}}$) are reproduced by the power amplifier.

The current flowing among μG1, μG2, and μG3 (i_{Net}) is the sum of $i_{\mu\text{G1,2}}$ and $i_{\mu\text{G1,3}}$, which is also reproduced by the power amplifier. It is found that the variations in the current PHIL experiments are similar to those expected in the simulation. The voltage of VSI in the different μGs is shown in Fig. 19(e). The voltages of $\text{VSI}_{\mu\text{G1}}$ ($V_{\text{ac},\mu G1}$), $\text{VSI}_{\mu\text{G2}}$ ($V_{\text{ac},\mu G2}$), and $\text{VSI}_{\mu\text{G3}}$ ($V_{\text{ac},\mu G3}$) are shown to be stable under the conditions of changing power exchange between μGs. The operation of the proposed control strategy in Scenario 2 is shown in Fig. 20. Similar to those expected in the simulation results, the power exchange is inversely proportional to the SOCs of the respective μGs. The variations in the $\text{V}_{\mu\text{G1}}$, $\text{V}_{\mu\text{G2}}$, and $\text{V}_{\mu\text{G3}}$ are demonstrated in Fig. 20(c) and are similar to those in the simulation study. The variations in the SOCs and current waveforms are also shown in Fig. 20(b) and (e), respectively. The 20 V in Fig. 20(b) in SOC denotes 20% of SOC. Fig. 21 depicts the operation of the proposed controller in Scenario 3 using PHIL experiments. The power exchange between the μGs is shown in Fig. 21(a). $P_{\mu G1,2}$ and $P_{\mu G1,3}$ are inversely proportional to the SOC value of the ESS and the MHL level of the hydrogen tank in the μGs. The 10 V in Fig. 21(b) for MHL denotes 10% of MHL, and the 20 V in Fig. 21(b) for SOC denotes 20% of SOC. Fig. 21(d) depicts the variations in current flowing through each μG in Scenario 3, which are similar to those expected in the simulation. Fig. 21(e) represents the VSI voltages for different μGs, and the enlarged figures demonstrate that the ac voltage waveforms are properly output through the power amplifier.

V. CONCLUSION

This article addresses a hierarchical (primary, secondary, and tertiary) power-sharing scheme in the μGs cluster especially based on the hybrid ESS. An adaptive MPC-based unified tertiary controller is proposed for the hybrid ESS-based μGs cluster for facilitating the SOC-based power distribution. All three hierarchical control layers (i.e., primary, secondary, and tertiary) are solved simultaneously, and the overall dynamic performance is presented. It was found that it is capable of facilitating all the set objectives while taking care of all operating conditions i.e., SOC limitations, rate of power change of power devices, and maximization of renewable power. The proposed control strategy provided the maximum overshoot of 9.02% in the dc bus which was found to be 15.02% using the conventional approach. In addition, using the proposed tertiary control method, the rate of power exchange among μGs can be smoothly controlled (100 W/s) corresponding to the FC operating modes in the respective μGs which is better for the FC lifetime. An interesting future research proposal can be developing and testing new variants of MPC such as hybrid models that can combine physics-based models with data-driven techniques to improve the accuracy and reduce the model complexity.

REFERENCES

[1] C. Bordons, F. Garcia-Torres, and M. A. Ridao, *Model Predictive Control of Microgrids*. Berlin, Germany: Springer, 2020.

[2] A. Hirsch, Y. Parag, and J. Guerrero, "Microgrids: A review of technologies, key drivers, and outstanding issues," *Renewable Sustain. Energy Rev.*, vol. 90, pp. 402–411, 2018.

[3] N. L. Díaz, A. C. Luna, J. C. Vasquez, and J. M. Guerrero, "Centralized control architecture for coordination of distributed renewable generation and energy storage in islanded AC microgrids," *IEEE Trans. Power Electron.*, vol. 32, no. 7, pp. 5202–5213, Jul. 2017.

[4] L. Meng et al., "Review on control of DC microgrids and multiple microgrid clusters," *IEEE J. Emerg. Sel. Top. Power Electron.*, vol. 5, no. 3, pp. 928–948, Sep. 2017.

[5] X. Lu, J. Lai, and X. Yu, "A novel secondary power management strategy for multiple AC microgrids with cluster-oriented two-layer cooperative framework," *IEEE Trans. Ind. Informat.*, vol. 17, no. 2, pp. 1483–1495, Feb. 2021.

[6] J. Lai, X. Lu, X. Yu, and A. Monti, "Cluster-oriented distributed cooperative control for multiple AC microgrids," *IEEE Trans. Ind. Inform.*, vol. 15, no. 11, pp. 5906–5918, Nov. 2019.

[7] X. Wu, Y. Xu, J. He, X. Wang, J. C. Vasquez, and J. M. Guerrero, "Pinning-based hierarchical and distributed cooperative control for AC microgrid clusters," *IEEE Trans. Power Electron.*, vol. 35, no. 9, pp. 9865–9885, Sep. 2020.

[8] P. Xie, Y. Jia, H. Chen, J. Wu, and Z. Cai, "Mixed-stage energy management for decentralized microgrid cluster based on enhanced tube model predictive control," *IEEE Trans. Smart Grid*, vol. 12, no. 5, pp. 3780–3792, Sep. 2021.

[9] X. Li et al., "Flexible interlinking and coordinated power control of multiple DC microgrids clusters," *IEEE Trans. Sustain. Energy*, vol. 9, no. 2, pp. 904–915, Apr. 2018.

[10] J. Zhou, H. Zhang, Q. Sun, D. Ma, and B. Huang, "Event-based distributed active power sharing control for interconnected AC and DC microgrids," *IEEE Trans. Smart Grid*, vol. 9, no. 6, pp. 6815–6828, Nov. 2018.

[11] Z. Zhao, P. Yang, Y. Wang, Z. Xu, and J. M. Guerrero, "Dynamic characteristics analysis and stabilization of PV-based multiple microgrid clusters," *IEEE Trans. Smart Grid*, vol. 10, no. 1, pp. 805–818, Jan. 2019.

[12] M. S. Golsorkhi, D. J. Hill, and H. R. Karshenas, "Distributed voltage control and power management of networked microgrids," *IEEE J. Emerg. Sel. Top. Power Electron.*, vol. 6, no. 4, pp. 1892–1902, Dec. 2018.

[13] S. Mudaliyar, B. Duggal, and S. Mishra, "Distributed tie-line power flow control of autonomous DC microgrid clusters," *IEEE Trans. Power Electron.*, vol. 35, no. 10, pp. 11250–11266, Oct. 2020.

[14] S. Moayedi and A. Davoudi, "Distributed tertiary control of DC microgrid clusters," *IEEE Trans. Power Electron.*, vol. 31, no. 2, pp. 1717–1733, Feb. 2016.

[15] Y. Han et al., "Coordinated power control with virtual inertia for fuel cell-based DC microgrids cluster," *Int. J. Hydrogen Energy*, vol. 44, pp. 25207–25220, 2016.

[16] B. John, A. Ghosh, M. Goyal, and F. Zare, "A DC power exchange highway based power flow management for interconnected microgrid clusters," *IEEE Syst. J.*, vol. 13, no. 3, pp. 3347–3357, Sep. 2019.

[17] L. Valverde, C. Bordons, and F. Rosa, "Integration of fuel cell technologies in renewable-energy-based microgrids optimizing operational costs and durability," *IEEE Trans. Ind. Electron.*, vol. 63, no. 1, pp. 167–177, Jan. 2016.

[18] F. Garcia-Torres, L. Valverde, and C. Bordons, "Optimal load sharing of hydrogen-based microgrids with hybrid storage using model-predictive control," *IEEE Trans. Ind. Electron.*, vol. 63, no. 8, pp. 4919–4928, Aug. 2016.

[19] Y. Shan, J. Hu, K. W. Chan, Q. Fu, and J. M. Guerrero, "Model predictive control of bidirectional DC-DC converters and AC/DC interlinking converters—A new control method for PV-wind-battery microgrids," *IEEE Trans. Sustain. Energy*, vol. 10, no. 4, pp. 1823–1833, Oct. 2019.

[20] Y. Shan, J. Hu, and J. M. Guerrero, "A model predictive power control method for PV and energy storage systems with voltage support capability," *IEEE Trans. Smart Grid*, vol. 11, no. 2, pp. 1018–1029, Mar. 2020.

[21] Y. Shan, J. Hu, M. Liu, J. Zhu, and J. M. Guerrero, "Model predictive voltage and power control of islanded PV-battery microgrids with washout-filter-based power-sharing strategy," *IEEE Trans. Power Electron.*, vol. 35, no. 2, pp. 1227–1238, Feb. 2020.

[22] Y. Shan, J. Hu, Z. Li, and J. M. Guerrero, "A model predictive control for renewable energy based AC microgrids without any PID regulators," *IEEE Trans. Power Electron.*, vol. 33, no. 11, pp. 9122–9126, Nov. 2018.

[23] X. Zhang, B. Wang, U. Manandhar, H. Beng Gooi, and G. Foo, "A model predictive current controlled bidirectional three-level DC/DC converter for hybrid energy storage system in DC microgrids," *IEEE Trans. Power Electrons.*, vol. 34, no. 5, pp. 4025–4030, May 2019.

[24] T. Dragičević, "Model predictive control of power converters for robust and fast operation of AC microgrids," *IEEE Trans. Power Electron.*, vol. 33, no. 7, pp. 6304–6317, Jul. 2018.

[25] Y. Han, K. Zhang, H. Li, E. A. A. Coelho, and J. M. Guerrero, "MAS-based distributed coordinated control and optimization in microgrid and microgrid clusters: A comprehensive overview," *IEEE Trans. Power Electron.*, vol. 33, no. 8, pp. 6488–6508, Aug. 2018.

[26] N. Vafamand, M. H. Khooban, T. Dragičević, and F. Blaabjerg, "Networked fuzzy predictive control of power buffers for dynamic stabilization of DC microgrids," *IEEE Trans. Ind. Electron.*, vol. 66, no. 2, pp. 1356–1362, Feb. 2019.

[27] V. Jayan, A. M. Y. M. Ghias, J. M. Guerrero, and A. Merabet, "An adaptive dynamic reference control for power converters in a microgrid," *IEEE Trans. Power Electron.*, vol. 37, no. 8, pp. 9164–9174, Aug. 2022.

[28] V. Jayan and A. M. Y. M. Ghias, "Computationally-efficient model predictive control of dual-output multilevel converter in hybrid microgrid," *IEEE Trans. Power Electron.*, vol. 38, no. 5, pp. 5898–5910, May 2023.

[29] B. Long et al., "Passivity-based partial sequential model predictive control of T-type grid-connected converters with dynamic damping injection," *IEEE Trans. Power Electron.*, vol. 38, no. 7, pp. 8262–8281, Jul. 2023.

[30] B. Long, J. Zhang, D. Shen, J. Rodríguez, J. M. Guerrero, and K. T. Chong, "Ultralocal model-free predictive control of T-Type grid-connected converters based on extended sliding-mode disturbance observer," *IEEE Trans. Power Electron.*, vol. 38, no. 12, pp. 15494–15508, Dec. 2023.

[31] R. Heydari et al., "Model-free predictive control of grid-forming inverters with *LCL* filters," *IEEE Trans. Power Electron.*, vol. 37, no. 8, pp. 9200–9211, Aug. 2022.

[32] J. Hu, Y. Shan, K. W. Cheng, and S. Islam, "Overview of power converter control in microgrids—Challenges, advances, and future trends," *IEEE Trans. Power Electron.*, vol. 37, no. 8, pp. 9907–9922, Aug. 2022.

[33] K. Kumar and S. Bae, "Coordinated dynamic power management for renewable energy-based grid-connected microgrids using model predictive control," *IEEE Trans. Ind. Informat.*, vol. 19, no. 9, pp. 9596–9608, Sep. 2023.

[34] Q. Shafiee, T. Dragičević, J. C. Vasquez, and J. M. Guerrero, "Hierarchical control for multiple DC-microgrids clusters," *IEEE Trans. Energy Convers.*, vol. 29, no. 4, pp. 922–933, Dec. 2014.

[35] A. Bemporad, N. Lawrence, and R. M. Morar, "Model predictive control toolbox$^{\mathrm{TM}}$ user's guide," R2024b. Mathworks, 2024. [Online]. Available: https://kr.mathworks.com/help/pdf_doc/mpc/mpc_ug.pdf

[36] I. Serban, S. Cespedes, C. Marinescu, C. A. Azurdia Meza, J. S. Gómez, and D. S. Hueichapan, "Communication requirements in microgrids: A practical survey," *IEEE Access*, vol. 8, pp. 47694–47712, 2020.

Kuldeep Kumar received the B.Tech. degree in energy engineering from the Maulana Azad National Institute of Technology, Bhopal, India, in 2012, and the M.Tech. and Ph.D. degrees in energy systems from the Department of Energy Science and Engineering, Indian Institute of Technology Delhi, New Delhi, India, in 2014 and 2019, respectively.

He is currently working as an Assistant Professor with the Indian Institute of Technology Guwahati, Guwahati, India. He worked as a Postdoctoral Researcher with the Electrical Engineering Department, Hanyang University, Seoul, South Korea. He also worked as a Research Associate with the School of Electrical, Computer and Telecommunications Engineering, University of Wollongong, Wollongong, NSW, Australia. His research interests include renewable energy grid integration, model predictive control, reinforcement learning, hybrid energy storage, fuel cells systems, modeling and control of converters and inverters, and control and optimization of microgrid/smart grid.

Chaeeun Lee received the B.S. degree in electrical engineering from the Hanyang University, Seoul, South Korea, in 2021. She is currently working toward the combined M.S. and Ph.D. degrees in electrical engineering with the Hanyang University, Seoul, South Korea.

Her research interests include energy conversion with renewable energy sources, energy management, and high-efficiency power converters.

Sungwoo Bae (Member, IEEE) received the B.S. degree in electrical engineering from the Hanyang University, Seoul, South Korea, in 2006, and the M.S.E. and Ph.D. degrees in electrical engineering from the University of Texas at Austin, Austin, TX, USA, in 2009 and 2011, respectively.

From 2012 to 2013, he was a Senior Research Engineer with the Power Center, Samsung Advanced Institute of Technology. From 2013 to 2017, he was a Professor with the Department of Electrical Engineering, Yeungnam University, Gyeongsan, South Korea. Since 2017, he has been a Professor with the Department of Electrical Engineering, Hanyang University, Seoul, South Korea.

Dr. Bae was the recipient of the Grand Prize by the Minister of Trade, Industry, and Energy of the Republic of Korea at the National Electrical Engineering Design Contest, in 2005.